Advanced applications of the EISCAT incoherent scatter radar for multi-beam and electron line studies

Mikael Hedin

IRF Scientific Report 277
June 2002

ISSN 0284-1703

INSTITUTET FÖR RYMDFYSIK
Swedish Institute of Space Physics

Kiruna, Sweden

Advanced applications of the EISCAT incoherent scatter radar for multi-beam and electron line studies

by

Mikael Hedin
Swedish Institute of Space Physics
P.O. Box 812, SE-981 28 Kiruna, Sweden

IRF Scientific Report 227
June 2002

Printed in Sweden
Swedish Institute of Space Physics
Kiruna 2002
ISSN 0284-1703

Typset with LaTeXby the author

IRF Scientific Report 277
ISSN 0284-1703
Printed at the Swedish Institute of Space Physics, Kiruna, 2002

Contents

Chapter 1

Introduction

This thesis investigates certain aspects of space physics, by which we mean the physics of the near earth space. The region closest to the surface of the earth, say below 1000 km altitude, is called the ionosphere. From the perspective of a distant observer and also compared with the earth's radius, 6370 km, the ionosphere is a very thin layer surrounding the earth. Most spectacular events take place in the lowest parts of this layer, say around 100 km. Continuing just a little bit further downwards, we enter the atmosphere proper, where space physics is no longer applicable.

The ionosphere is strongly influenced by the magnetosphere, which is in turn influenced by the solar wind. In that sense, the topic of the ionosphere does have a firm connection to what we on a daily basis consider to be "space".

This reports starts with a brief introduction to the ionosphere, where some background will be given. We will then continue with a description of incoherent scatter radars in general. Some topics that are more relevant will be covered in more detail, while others will be treated very briefly. For a deeper understanding of the subject, the interested reader is urged to follow the references where a more comprehensive treatment is found.

The last part of this report introduces the three papers, where some different aspects of ionospheric physics are treated.

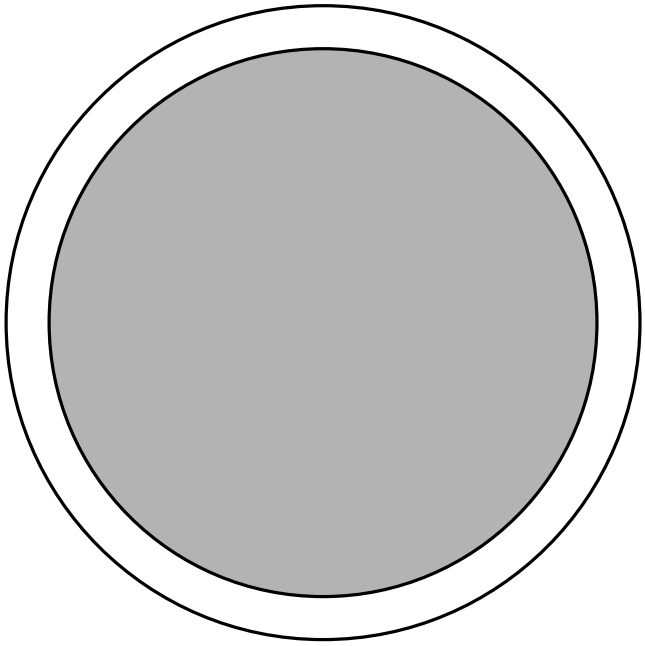

Figure 1.1: Model of the earth (shaded) and an altitude of 1000 km

Chapter 2

The ionosphere

2.1 A brief treatment

The earliest evidence of the ionosphere is from the 19-th century. Auroral studies had led to the conclusion that there were currents in the upper atmosphere, assumed to be produced by influence of solar heating.

The successful radio transmission over the Atlantic Ocean early in the 20-th century was further evidence for a conducting atmospheric layer. It was originally called the Kenelly-Heaviside layer, after the two scientists who independently postulated its existence in order to explain the transatlantic radio transmission. When the first direct probings of this layer were performed by Appleton, he labeled it the E-layer for the electric wave vector. Later more conducting layers were discovered, and as all these layers are produced by ionization of the neutral atmosphere, the whole region was eventually named the ionosphere.

Today, the ionosphere is characterized as the ionized part of the upper atmosphere, from the altitude where the ionization conceivably influences the dynamics of the gas, to where the density is so low that there are no longer any gas characteristics left but only particle populations. The ionospheric boundaries depend strongly on the conditions at the specific geographic location. Following the amount of sunlight and particle precipitation, the density of free charges varies considerably with location, season and time of the day.

The ionosphere is divided into three distinct regions, from lower to higher altitudes called the D-, E- and F-region respectively. Two of these are present in the density profile in figure 2.1 over a typical range of the strongest part of the ionosphere, from 100 to 700 kilometers.

2.2 On the ionospheric density

The most significant property of the ionosphere is the abundance of charged particles, free electrons and ions. The density of the free electrons is called the ionospheric density, or just electron density. It is the most often used parameter measured by incoherent scatter radars. In the following I will describe some factors that influence this density.

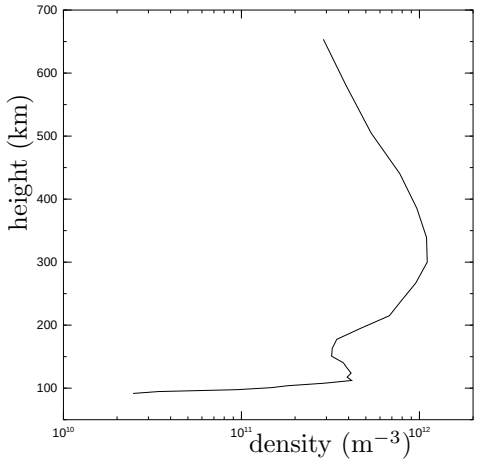

Figure 2.1: A typical electron density profile as measured by EISCAT 2001-10-08 in Tromsø. The lowest peak is the E-region, and the much broader peak above 200 km is the F-region. In this measurement, the D-region is not probed.

The source of matter to ionize is the ambient neutral atmosphere. The ionospheric density will depend on the neutral density and on the rate of production and loss of ionization. The upper atmosphere usually obeys the hydrostatic equation, which means that the density of neutral constituents of the atmosphere decreases exponentially with height h,

$$n = n_0 e^{-(h-h_0)/H}, \tag{2.1}$$

where $H = kT/mg$ is the scale height. There is not enough particle collisions in this region to mix the species, so there will be separate scale heights for each species. The scale height depends on the particle mass in such a way that light particles will have a greater scale height and thus their density decreases slower with increasing altitude. A typical value for oxygen is 50 km. This means that at high altitudes, light constituents like hydrogen will dominate.

The ionization caused by solar radiation, on the other hand, is usually strongest at high altitudes: the incident flux from the sun will reach the top of the atmosphere first, and as it ionizes the atoms, the flux will decrease. The result is that the ionization will have a peak somewhere where the density and ionization combines to a maximum. Using a simple model, called a Chapman model, the ionization production for a single species will be

$$Q = Q_0 \exp(1 - y - e^{-y}) \tag{2.2}$$

where $y = (h - h_m)/H$. The ionization produced by precipitation is a bit more complicated to calculate, as there will be secondary particle production, bremsstrahlung, *etc.* to consider. Empirical studies have shown how the energy is deposited in the neutral gas, *e.g.,* Rees (1963).

Finally, the loss of ionization has to be determined. Different types of recombination will occur, but the net result is that one electron and one ion are converted into neutrals. For ion and electron density n_e and n_i, the rate of this reaction is

$$L = \alpha n_\mathrm{e} n_\mathrm{i}, \tag{2.3}$$

where the recombination coefficient α for different reactions can be found in the aeronomy literature, *e.g.,* Banks and Kockarts (1973).

If we now want to calculate the ionospheric density, we have to put all these equations into a general continuity equation:

$$\frac{\partial n_{\mathrm{e}}}{\partial t} + \nabla n_{\mathrm{e}} = Q - L. \tag{2.4}$$

To solve this equation, various assumptions about the plasma transport must be made, and the resulting equation will often be a candidate for numerical simulations. Even so, a solution for a simplified model atmosphere gives a qualitatively correct solution.

For more details and in-depth description of the ionosphere, refer to standard textbooks in space physics, *e.g.,* Kivelson and Russell (1995).

Chapter 3

Incoherent scatter radars

It was proposed by Gordon (1958) that it should be possible to utilize the incoherent scatter of a strong radio wave from electrons to probe the ionosphere. The scatter was soon confirmed by Bowles (1958), but the received signal was much stronger than expected. The original proposition had only considered free electrons, but the plasma properties of the ionosphere proved to be all important: the electron motions are controlled by the ions present. This leads to the useful technique of incoherent scatter radars, which have now developed into a standard method to explore the ionosphere.

The fundamental physical process responsible for the incoherent scatter is Thomson scattering, *i.e.,* scattering of electromagnetic waves by free electrons. The electrons in the ionosphere exhibit individual thermal motion, so the return signal will consist of the signals from individually moving targets, hence the term incoherent scatter—the actual scatter is however coherent. By contrast, a traditional radar uses the echo from a single object, a hard target scatter, that reflects the wave unaltered, *i.e.,* a coherent scatter.

The radars required have a large transmitting power and a sensitive receiver, which leads to rather large installations. Today there are several radars installed around the earth, mostly in the northern hemisphere, operating on a regular basis.

3.1 Incoherent scatter theory

Appendix A describes how the radiation scattered from an incident harmonic wave is derived. The power spectrum of the return signal is shown to be

$$|E_r(\omega)|^2 = \sin^2\delta \frac{\vec{E_0}^{\,2}}{\vec{R}_\mathrm{i}^2 \vec{R}_\mathrm{s}^2} r_\mathrm{e}^2 \left|\Delta N(\omega-\omega_0)\right|^2, \tag{3.1}$$

where E_r is the electric field of the return signal, δ is the scattering angle (90 degrees for back scatter), $\vec{E_0}$ is the transmitted electric field maximum, $\vec{R}_\mathrm{i}$ and $\vec{R}_\mathrm{s}$ are the distances from the transmitting and receiving antenna to the scattering point, r_e is the classical electron radius, ΔN is the deviation of the electron density from its mean density and ω_0 is the transmitting angular frequency. As the measured quantity, $\vec{E_\mathrm{r}}(t)$, is a superposition of constituents

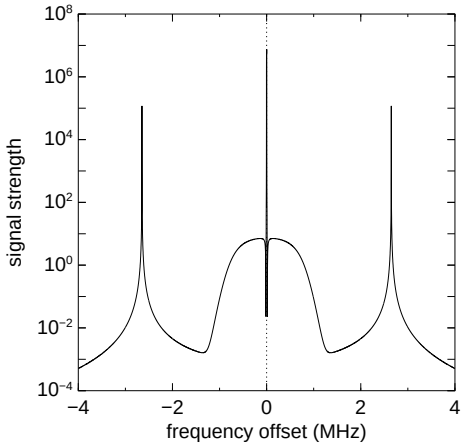

Figure 3.1: The incoherent scatter power spectrum. In the middle is the narrow ion line, and the wide but faint electron line, and at the edges the two plasma lines.

from incoherent, or stochastic, motions, it will itself be a random fluctuation; only by using the power spectrum it will be possible to use the information.

To make use of equation (3.1), we need to know how $|\Delta N(\omega)|^2$ depends on the physical parameters. This can be derived using fundamental equations for the particle motions in the plasma, *e.g.,* the Vlasov equation, a differential equation for the distribution function f:

$$\frac{\partial f}{\partial t} + \vec{v} \cdot \nabla + \vec{a} \cdot \nabla_v f = 0 \tag{3.2}$$

where $\vec{v}$ and $\vec{a}$ are the bulk velocity and acceleration of the plasma respectively.

One method for doing this is to use the Nyquist theorem (Nyquist, 1928) as described in Paper III. This theorem determines the spontaneous thermal fluctuations for a general dissipative system, derived from the dynamic properties of the system. An advantage of this method is that the stochastic nature of the thermal motion in the plasma is built into the theorem, and does not have to be treated explicitly. We arrive at

$$\langle|\Delta N(\omega)|^2\rangle = |r_e R|^{-2} \sum_e \left\{ \left| R - \frac{{q_e}^2 N_e y_e}{T_e} \right|^2 \frac{N_e y_e^R}{\omega} + \left| \frac{q_e N_e y_e}{T_e} \right|^2 \left(S - \frac{{q_e}^2 N_e y_e^R}{\omega} \right) \right\}, \tag{3.3}$$

with symbols as defined in Paper III. A typical spectrum is shown in figure 3.1, where we see the central ion line, the broad but weak electron line and on the flanks the two plasma lines. With a higher resolution, the ion line looks as in figure 3.2. The central ion line is the main signal. It is narrow as the electrons are bound to the ions, and with the high ion mass they give a small thermal Doppler broadening. These electrons have a low energy. The two shoulders of the ion line are associated with approaching and leaving ion

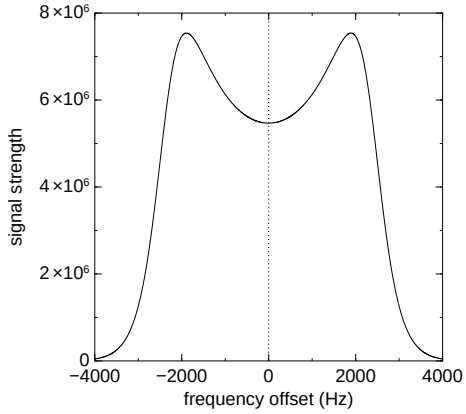

Figure 3.2: An enlarged view of the ion line.

acoustic waves. The shape of the ion line depends on the plasma parameters roughly as follows: the spectral height is the electron density, the first moment is the plasma drift velocity, the width depends on the ion temperature and the depression in the middle depends on electron temperature and collision frequency. The electron line is the scatter from electrons not bound to ions, with enough energy to stay free from the ion influence, some electron volts. Its width depends on the electron temperature, and the strength is sensitive to small changes in the electron distribution function in the corresponding energy interval. The plasma lines are from the approaching and leaving Langmuir waves, with electron energies in the range of ten electron volts. The Langmuir frequency, and hence the plasma line frequency offset, is closely related to the plasma density. The whole spectrum will be Doppler shifted if there is a bulk motion of the plasma parallel to the beam direction.

The use of the Nyquist theorem was pioneered early in a series of articles (Dougherty and Farley (1960); Farley et al. (1961); Dougherty and Farley (1963); Farley (1966); Swartz and Farley (1979)) and the reader is referred to them for a detailed description of the derivations.

3.2 Incoherent scatter practicals

To realize the incoherent scatter radar, the measured electric field must be subject to some signal processing. From general theorems on Fourier transforms, the relation between a time series $x(t)$ and a frequency spectrum $X(\omega)$ is

$$\mathcal{F}^{-1}\{|X(\omega)|^2\} = \mathcal{A}\{x(t)\} \tag{3.4}$$

where $\mathcal{F}^{-1}$ denotes the inverse Fourier transform,

$$x(t) = \mathcal{F}^{-1}\{X(\omega)\} = \int_{-\infty}^{\infty} X(\omega) e^{i\omega t}\, \mathrm{d}\omega, \tag{3.5}$$

and $\mathcal{A}$ the autocorrelation,

$$\mathcal{A}\{x(t)\} = \int_{-\infty}^{\infty} x^*(t) x(t-\tau)\, \mathrm{d}t. \tag{3.6}$$

Note that the Fourier transform converts between domains, *e.g.,* the time domain and the frequency domain, but the autocorrelation stays in the same domain. The free variable of the autocorrelation function is often called the lag, as it indicates a difference in time. It is a measure of the randomness of the signal; a random signal will have a random and very small autocorrelation for all lags except zero.

To measure the frequency spectrum of the incoherent scatter return signal, the received electric field, $E(t)$, is sampled during a limited amount of time. Call the samples E_t. The autocorrelation for a specific lag τ is then approximated as the summation of the lag product of the samples, $\sum_t E_t^* E_{t-\tau}$. In principle this summation is for all t, but in practice it is limited to some probing interval, typically 5 seconds.

We then calculate the inverse Fourier transform of the theoretical spectrum as a function of physical parameters. Varying these parameters, the theoretical and measured autocorrelation functions are fitted and thus the conditions of the probed ionospheric volume can be inferred. Alternatively, we could make the Fourier transform of the probed autocorrelation function, and compare with the theoretical spectrum.

3.3 Pulse coding

If we just transmit and receive with a single antenna (a mono-static radar), the received signal will contain information from a range in the radial direction corresponding to the length on the transmit period (the volume integration in equation (A.14) will be bounded in the radial direction by the start and end of the transmitted pulse). If we want to probe a certain volume in the ionosphere, we will thus have to transmit in pulses of appropriate length. This will be what is called a short pulse experiment. To make more efficient use of the radar, methods to transmit more frequent pulses and make measurements for several heights simultaneously have been developed, using different kinds of pulse coding techniques.

To understand the use of pulse coding, the concept of *ambiguity functions* has been developed (*e.g.,* Lehtinen, 1986). The full ambiguity function is a measure of how much information is included in a specific measurement depending on lag and range. The easiest to illustrate is the *range ambiguity function*, a reduced ambiguity function which only concerns from what ranges (or heights) the information is collected.

There is a separate ambiguity function for each measured lag product. By using the range ambiguity function, we can deduce which lag products come from the same range, and collect them to use in the autocorrelation function estimate. The easiest code used is a simple pulse code, pulses sent at certain intervals. We describe the transmitted signal by its envelope. A simple pulse code (1,3,2) will have an envelope as shown in figure 3.3. The numbers correspond to the gaps between consecutive pulses.

The range ambiguity function is the product of the convolution of the envelope e and the receiver impulse response h for the two times involved,

$$W_{tt'}^r = (h * e)(t) \cdot (h * e)(t'). \tag{3.7}$$

The range ambiguity function for the (1,3,2) code is shown in figure 3.4 for a

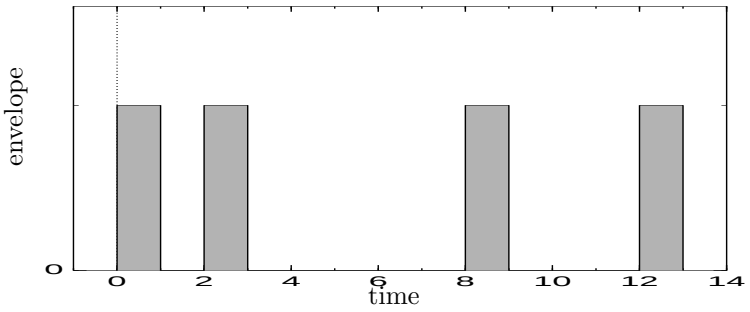

Figure 3.3: Envelope of (1,3,2) pulse code.

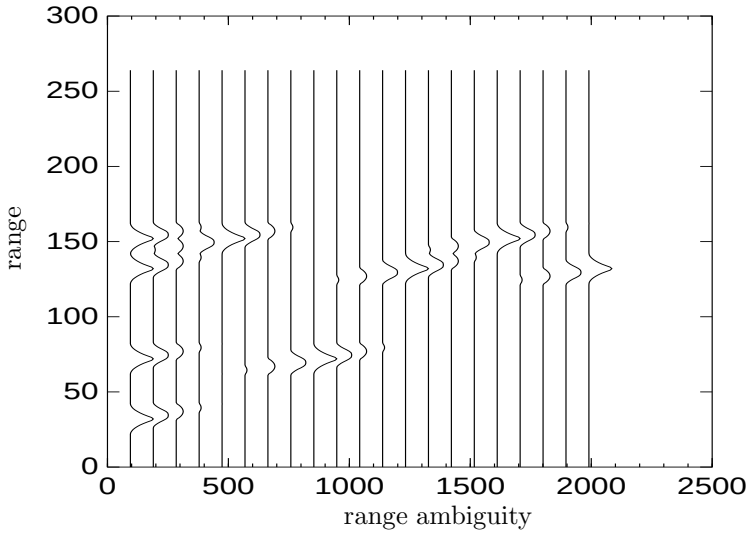

Figure 3.4: Range ambiguity function for fractional lags of pulse code (1,3,2) in arbitrary units. The successive lags are staggered along the abscissa for visibility.

fractionality of 4, *i.e.,* every 4-th lag corresponds to an inter-pulse interval. It is clearly seen that the full lags give the most confined peaks, while the fractional lags have different degrees of wider spread, or ambiguity. The leftmost line is the zero-lag, which is never used in pulse code experiments as it is non-zero for several ranges, corresponding to the transmitted envelope.

An alternative method is Barker coding. It is an application of phase coding, *i.e.,* the phase of the transmitter is changed by π, or equivalently the envelope is changed between 1 and -1. A 13-bit Barker code is shown in figure 3.5. By using receiver filters with an impulse response equivalent to the transmitted pulse, the ambiguity function can be made very narrow. This means that the transmitted power is confined to a small part of the signal length, in this case a 13-th of the total pulse length, and thus this is sometimes called pulse compression. As the impulse response of the receiver filter is equivalent to the transmitted pulse, it is also called matched filter code.

A newer method is alternating codes (Lehtinen and Häggström, 1987). These

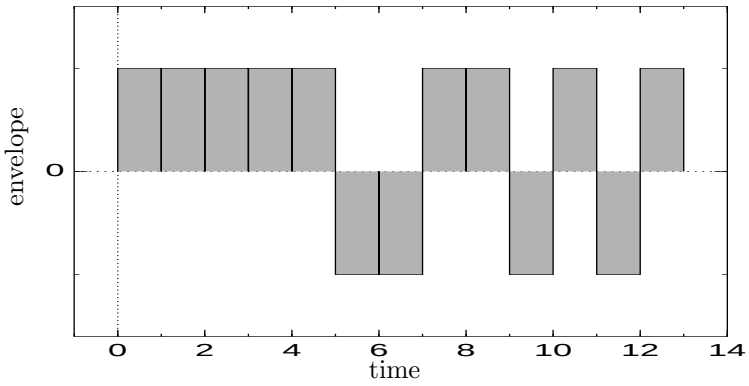

Figure 3.5: Envelope of 13-bit Barker code

are constructed from mathematically defined sequences of phase codes. By combining data from the sequences in different ways, information from any chosen sub-interval of the total pulse length can be extracted. This makes it easier to make high-resolution measurements while keeping a signal level above the background noise level. These code sequences have to be carefully designed to achieve the desired effect, and a limitation is that the whole sequence (up to one second) must be run through under the same ionospheric micro-condition. Thus the method cannot be applied to very fast varying or transient effects.

Today, most standard incoherent scatter experiments use some pulse coding technique to use the radar in the most efficient way possible.

3.4 The EISCAT facility

All experiments used in the present work use the European Incoherent SCATter facility (EISCAT). Today, there are two EISCAT systems in operation: the mainland system in Kiruna, Sodankylä and Tromsø (the KST system) and the EISCAT Svalbard Radar (ESR) located in Longyearbyen. The mainland system has a mono-static, meridionally steerable VHF radar (224 MHz) in Tromsø, and a tri-static, fully steerable UHF radar (931 MHz) with transmitter in Tromsø and receivers in Kiruna, Sodankylä and Tromsø. The ESR system is a UHF radar (500 MHz) with a dual antenna system, one fixed in a direction aligned with the magnetic field lines, and one fully steerable, with a split feed system alternating between the antennas.

In the time between Paper I and Paper III, the hardware has changed from a custom analog electronic system towards a software based digital system, which has greatly improved the system characteristics and enabled a more flexible use of the radar, *e.g.,* as the experiment used in Paper III. Some more data for the current system are shown in table 3.1.

Location	Tromsø		Kiruna	Sodankylä	Longyearbyen
Band	VHF	UHF	UHF	UHF	UHF
Frequency	224 MHz	931 MHz	931 MHz	931 MHz	500 MHz
Bandwidth	3 MHz	8 MHz	8 MHz	8 MHz	10 MHz
Channels	8	8	8	8	6
Phase coding	binary				
Transmitter	2 klystr	2 klystr			8 klystr
Peak Power	2×1.5 MW	1.5 MW			500 kW
Average Power	2×150 kW	150 kW			125 kW
Pulse Duration	1 μs–2 ms	1 μs–2 ms			1 μs–2 ms
Min interpulse	1.0 ms	1.0 ms			0.1 ms
Receiver	analog-digital				
Digital Processing	14-bit 15MHz ADC lag profiles 32-bit complex				12-bit 10MHz ADC lag profiles 32-bit complex
System Temperature	250–350 K	90–110 K	30–35 K	30–35 K	80–85 K
Antenna	4 30×40 m parabolic cylinders	32 m parabolic dish	32 m parabolic dish	32 m parabolic dish	32 m and 42 m parabolic dish
Feed system	line feed	Cassegrain	Cassegrain	Cassegrain	Cassegrain
Gain	46 dBi	48.1 dBi	48.1 dBi	48.1 dBi	42.5 dBi or 44.8 dBi
Polarization	circular	circular	any	any	circular
System merit figure	30 MWm^2/K	8 MWm^2/K			3 MWm^2/K

Table 3.1: Specification of the EISCAT radars

Chapter 4

Included papers

4.1 Paper I

This paper, Hedin et al. (2000), uses an experiment performed in 1997. It is a large coordinated study, using the FAST satellite (Carlson et al., 1998), EISCAT mainland (Folkestad et al., 1983) and Svalbard (Wannberg et al., 1997) radars and the ALIS facility (Brändström and Steen, 1994). Here we use standard modes of operation for all the radars, but use them simultaneously in a new geometric configuration: a wide-latitude meridional fan pattern with four beams covering 10–20 degrees in latitude. During this time, the ESR radar had only one antenna, the other beams are the mainland VHF antenna in a meridional split-beam mode and the UHF antenna.

During the experiment, the main ionospheric trough passed through all the radar beams. The trough is characterized by a significant depletion of electrons, an empty region without much activity. Meanwhile, FAST passed over the region probed by the radars, and we can see how the satellite data agrees with the radar density measurements. ALIS measurements were partly prevented by cloudy weather, but when the edge of the trough passed ALIS, there was some diffuse aurora, as expected from earlier experiments. To summarize, no exciting events took place during this observation, but it has shown how the radars can be used together as a wide latitude scanning meta-radar, covering large areas in a way normally not possible to probe with incoherent scatter radars. This gives a totally new amount of detail in the measurement resolution, over a range normally associated with HF-radars, which have a completely different range of resolution.

4.2 Paper II

This paper, Häggström et al. (2000), uses measurements made during the Swedish and Japanese joint EISCAT-ALIS campaign February 1999. The original objective was to measure inside auroral arcs with the EISCAT UHF system using ALIS snapshot images to aim at relevant positions with all three radars. However, it turned out that all the allocated days were cloudy, so it was not possible to actually do this. The radars were instead run in a fixed field-aligned position. The radar experiment for Tromsø was a special purpose combination

of ion and plasma line measurements, using both the UHF and VHF signal processing hardware, fed from the UHF receiver system. This produced two datasets, one for the common ionospheric plasma parameters, and one for the plasma line measurements.

For the analysis of the data, an extension to the theoretical incoherent scatter spectrum function was proposed. This extension takes into account that the condition of a Maxwellian electron distribution fails to be true even under common conditions. The spectrum function proposed has a simple extension for a summation over several Maxwellian electron distributions:

$$S(f) = \frac{1}{\pi} \cdot \frac{\left|\sum_e \frac{N_e y_e}{T_e}\right|^2 \sum_i \frac{n_i Z_i^2 \Re(y_i)}{f + k v_i / 2\pi} + \left|jC_D + \sum_i \frac{n_i Z_i^2 y_i}{T_i}\right|^2 \sum_e \frac{N_e \Re(y_e)}{f + k v_e / 2\pi}}{\left|\sum_e \frac{N_e y_e}{T_e} + jC_D + \sum_i \frac{n_i Z_i^2 y_i}{T_i}\right|^2} \quad (4.1)$$

with symbols as defined in Paper II. This was used to explain the observed strength of different plasma lines. It was concluded that this can be due to up- or down-going supra-thermal electrons, in this case with an inferred current of $12\,\mu\mathrm{A/m}^2$ ampère.

4.3 Paper III

This paper, Hedin and Häggström (2002), further investigates the question of the spectrum function presented in Paper II. The derivation starts from micro-physical conditions, and arrives at a modification of equation (4.1):

$$\langle |\Delta N(\omega)|^2 \rangle = |r_e R|^{-2} \sum_e \left\{ \left| R - \frac{{q_e}^2 N_e y_e}{T_e} \right|^2 \frac{N_e y_e^R}{\omega} + \left| \frac{q_e N_e y_e}{T_e} \right|^2 \left(S - \frac{{q_e}^2 N_e y_e^R}{\omega} \right) \right\} \quad (4.2)$$

with symbols as defined in the paper. The necessary conditions are considered in this paper, and an important one is that the electron distribution deviation from a Maxwellian must be small in some sense for the derivation to be valid. There is also a condition on local thermodynamic equilibrium, which cannot be strictly fulfilled, but the use is nevertheless plausible because of the adiabatic changes we are concerned with—the measurement time scale is normally much smaller than the time scale of thermodynamic changes.

The new function for the incoherent scatter spectrum can be used for an electron distribution modified by inelastic electron neutral collisions. The result suggests a large enhancement of the electron line, as shown in Gustavsson et al. (2001).

Two EISCAT campaigns were carried out to investigate this relation during 2001, in March and October. The results from these campaigns are compared with spectra for conditions that are expected during HF-pumping. The normal procedure of fitting measured spectra with theoretical ones is not really applicable, as this is the first time such experiments have been performed. We must first deduce if the electron line is visible at all, and if so, how it can be fitted to the theory.

With the current EISCAT hardware, the electron line signal should be just over the limit for detection, which makes the analysis harder. The Arecibo radar should be more suitable for this kind of measurements, but there is no HF-pumping facility and the transmitting frequency makes the electron line weaker.

Appendix A

Derivation of the scattered radiation

We will derive the basic function for studies of ionospheric incoherent scatter, the power spectrum of the signal scattered from a volume of plasma. The basic reaction is Thomson scattering, electromagnetic radiation scattered by free electrons.

The electric field produced by an charged particle accelerated by $\dot{\vec{\beta}} = \dot{\vec{v}}/\mathrm{c}_0$, observed at distance R in direction $\hat{n}$ is given by (*e.g.,* Jackson, 1975)

$$\vec{E} = \frac{1}{4\pi\varepsilon_0}\frac{q}{\mathrm{c}_0}\left[\frac{\hat{n}\times(\hat{n}\times\dot{\vec{\beta}})}{R}\right]_{\mathrm{ret}} \tag{A.1}$$

where q is the charge, and the expression in brackets is evaluated at the retarded time, $t - R/\mathrm{c}_0$. If we choose a coordinate system such that $\dot{\vec{\beta}} \parallel \hat{y}$ and $\hat{n}\cdot\hat{z} = 0$, then $\hat{n}$ is in the x–y plane. We define the angle between $\hat{n}$ and $\hat{y}$ as δ. Then

$$\hat{n}\times\dot{\vec{\beta}} = \sin\delta|\dot{\vec{\beta}}|(\hat{x}\times\hat{y}) = \sin\delta|\dot{\vec{\beta}}|\hat{z} \tag{A.2}$$

and

$$\hat{n}\times(\hat{n}\times\dot{\vec{\beta}}) = \sin\delta|\dot{\vec{\beta}}|\hat{n}\times\hat{z} = \sin\delta|\dot{\vec{\beta}}|\hat{m} \tag{A.3}$$

where

$$\hat{m}\cdot\hat{z} = 0 \tag{A.4}$$

$$\hat{m}\cdot\hat{n} = 0 \tag{A.5}$$

$$|\hat{m}| = 1. \tag{A.6}$$

We can also write $\hat{m} = \cos\delta\hat{x} - \sin\delta\hat{y}$. Using these symbols, equation (A.1) can be written

$$\vec{E} = \frac{\hat{m}}{4\pi\varepsilon_0}\frac{q}{\mathrm{c}_0}\sin\delta\left[\frac{|\dot{\vec{\beta}}|}{R}\right]_{\mathrm{ret}}. \tag{A.7}$$

Consider an incident electro-magnetic wave with electric field strength $\vec{E}_{\mathrm{i}}$. (We ignore the magnetic field as this will be a second order effect, $\vec{v}\cdot\vec{B}$). The charge will then move as

$$m\dot{\vec{v}} = q\vec{E}_{\mathrm{i}} \tag{A.8}$$

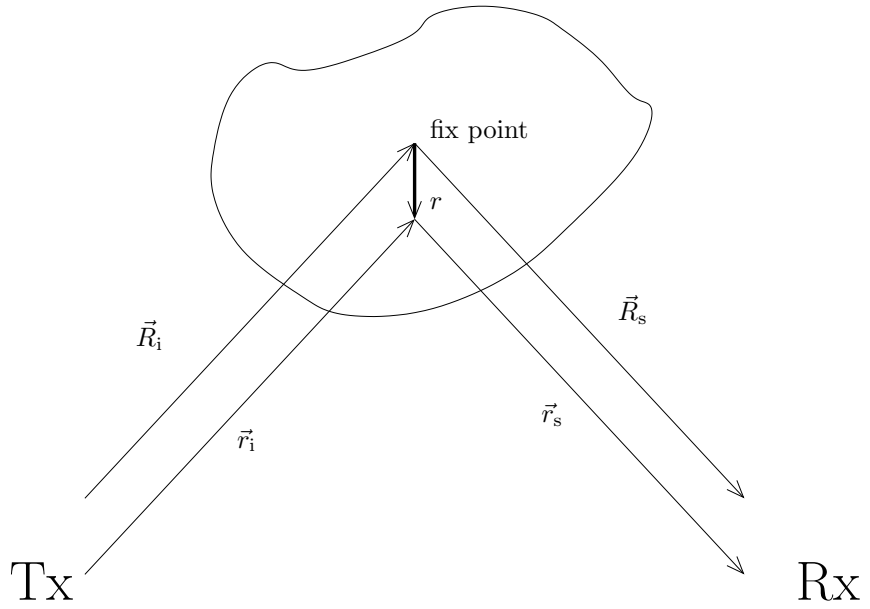

Figure A.1: Symbols used in the scattering theory

and the scattered radiation is

$$\vec{E}_\mathrm{s} = \hat{m}\frac{q^2}{4\pi\varepsilon_0 m c_0^2}\sin\delta\left[\frac{|\vec{E}_\mathrm{i}|}{R}\right]_\mathrm{ret} \tag{A.9}$$

or if we consider electrons at $\vec{x}_0$ and use the classical electron radius $r_\mathrm{e} = e^2/4\pi\varepsilon_0 m_\mathrm{e} c_0^2$

$$\vec{E}_\mathrm{s}(\vec{r},t) = \hat{m} r_\mathrm{e}\sin\delta\frac{|\vec{E}_\mathrm{i}(\vec{x}_0(t'),t')|}{|\vec{r}-\vec{x}_0(t')|}. \tag{A.10}$$

where we use the retarded time $t' = t = R/\mathrm{c}_0$. We assume that the scattered radiation does not infer the incident one (the Born approximation). Note that $\delta = 90°$ is forward and backward scattering, and $\delta = 0$ is perpendicular, which gives no scatter.

If we have a transmitter $\vec{E}_\mathrm{tx} = \vec{E}_0 e^{i(\omega_0 t+\phi_0)}$, the radiation incident on a long distance is

$$\vec{E}_\mathrm{i} = \frac{\vec{E}_0}{\vec{r}_\mathrm{i}} e^{i(\omega_0 t - \vec{k}_\mathrm{i}\cdot\vec{r}_\mathrm{i}+\phi_0)}. \tag{A.11}$$

where in general the distance $\vec{r}_\mathrm{i}$ and the wave number $\vec{k}_\mathrm{i}$ are perpendicular. In practice the distance used will always be very long, typically 100 km, compared to the wavelength, typically 1 m, so this is not a serious restriction.

When used in practice, the return signal will be the sum of the signal from all the charges in the scattering volume, the volume covered by the radar beam. It is determined by the antenna pattern, but if we assume that the physical conditions are constant throughout the volume this can be replaced with a fixed volume.

We now use auxiliary variables according to figure A.1, such that r is the distance from an arbitrary but fixed point in the scattering volume. Then

$\vec{r}_\mathrm{i} = \vec{R}_\mathrm{i} + r$ and $\vec{r}_\mathrm{s} = \vec{R}_\mathrm{s} - r$. Using these variables the phase of $\vec{E}_\mathrm{s}$:s can be written

$$\begin{aligned}\Theta &= \omega_0 t - (\vec{k}_\mathrm{i} - \vec{k}_\mathrm{s}) \cdot \vec{r} - \vec{k}_\mathrm{i} \cdot \vec{R}_\mathrm{i} - \vec{k}_\mathrm{s} \cdot \vec{R}_\mathrm{s} + \phi_0 \\ &= \omega_0 t - \vec{k} \cdot \vec{r} + \theta_0\end{aligned} \tag{A.12}$$

where

$$\vec{k} = \vec{k}_\mathrm{i} - \vec{k}_\mathrm{s}. \tag{A.13}$$

Note that θ_0 only depends on the experiment geometry and for the common case of backscatter $\vec{k} = 2\vec{k}_\mathrm{i}$. The received signal $\vec{E}_\mathrm{r}$ is then

$$\vec{E}_\mathrm{r}(t) = \int_{V_s} \vec{E}_\mathrm{s}(\vec{r}, t) N(\vec{r}, t') \, \mathrm{d}^3 r \tag{A.14}$$

where $\vec{r}$ is calculated at the retarded time, and $N(\vec{r})$ is the free electron density. If we use a windowing function $w(\vec{r})$ to describe the antenna pattern instead of limiting the integration to V_s we can write

$$\begin{aligned}\vec{E}_\mathrm{r}(t) &= \int w(\vec{r}) \vec{E}_\mathrm{s}(\vec{r}, t) N(\vec{r}, t') \, \mathrm{d}d^3 r \\ &= \hat{m} \sin\delta \frac{\vec{E}_0}{\vec{R}_\mathrm{i}\vec{R}_\mathrm{s}} r_\mathrm{e} \int w(\vec{r}) N(\vec{r}, t') e^{i(\omega_0 t - \vec{k}\cdot\vec{r} + \theta_0)} \, \mathrm{d}^3 r.\end{aligned} \tag{A.15}$$

Here we assume $\vec{r}_\mathrm{i}, \vec{r}_\mathrm{s} \ggg V_s^{1/3}$ so that $\vec{r}_\mathrm{i} = \vec{R}_\mathrm{i}$ and $\vec{r}_\mathrm{s} = \vec{R}_\mathrm{s}$. Now write $N(\vec{r}, t)$ as $N_0 + \Delta N(\vec{r}, t)$ where N_0 is constant:

$$\begin{aligned}\vec{E}_\mathrm{r}(t) &= \hat{m} \sin\delta \frac{\vec{E}_0}{\vec{R}_\mathrm{i}\vec{R}_\mathrm{s}} r_\mathrm{e} e^{i(\omega_0 t - \theta_0)} \left[N_0 \int w(\vec{r}) e^{i\vec{k}\cdot\vec{r}} \, \mathrm{d}^3 r + \int w(\vec{r}) \Delta N(\vec{r}, t') e^{i\vec{k}\cdot\vec{r}} \, \mathrm{d}^3 r. \right] \\ &= \hat{m} \sin\delta \frac{\vec{E}_0}{\vec{R}_\mathrm{i}\vec{R}_\mathrm{s}} r_\mathrm{e} e^{i(\omega_0 t - \theta_0)} \left[N_0 W(\vec{k}) + W(\vec{k}) * \Delta N(\vec{k}, t') \right].\end{aligned} \tag{A.16}$$

As $w(\vec{r})$ is much greater than $\vec{k}$ and typical scale sizes of ΔN, $W(\vec{k})$ is narrow in $\vec{k}$ around $\vec{k} = 0$ and the convolution has a minor impact on ΔN. We write $\Delta\tilde{N} = W * \Delta N$, but often ΔN and $\Delta\tilde{N}$ will be used for the same purpose, even though they differ with a constant. Note that the convolution concerns $\vec{k}$-space. The first term, with N_0, can be ignored as $W(\vec{k})$ is narrow in $\vec{k}$ and significant only for forward scattering, which is not applicable for radars.

If we calculate the Fourier transform of the autocorrelation of $\vec{E}_\mathrm{r}$ (in the time dimension), we get a double sided spectrum for the received effect, or the scattering cross section:

$$\begin{aligned}|E_r(\omega)|^2 &= \mathcal{F}\left\{\mathcal{A}\left\{\vec{E}_\mathrm{r}\right\}\right\} = \sin^2\delta \frac{\vec{E}_0^{\,2}}{\vec{R}_\mathrm{i}^2\vec{R}_\mathrm{s}^2} r_\mathrm{e}^2 \mathcal{F}\left\{\mathcal{A}\left\{e^{i\omega_0 t}\Delta N(\vec{k}, t')\right\}\right\} \\ &= \sin^2\delta \frac{\vec{E}_0^{\,2}}{\vec{R}_\mathrm{i}^2\vec{R}_\mathrm{s}^2} r_\mathrm{e}^2 \left|\Delta N(\vec{k}, \omega - \omega_0)\right|^2.\end{aligned} \tag{A.17}$$

This is the classical result for incoherent scatter. It is used to compute how the spectrum depends on actual physical parameters, such as temperature and drift velocity.

Acknowledgements

Instead of trying to name all the people that deserves to be acknowledged in one way or another, and forgetting some, I will avoid most names. The biggest thanks goes to all the nice people I have come to know during the years in Kiruna. Without you all, it would of course not have been possible. I also want to thank my supervisors, Ingemar Häggström and Asta Pellinen-Wannberg—I know it has not always been an easy task. For help to prepare this text, I thank Björn Gustavsson and Parviz Haggi for valuable critics, comments and suggestions, and Rick McGregor for proof-reading. I cannot blame them for any misstakes remaining. I would also like to thank the Swedish Institute of Space Physics for paying my salary.

Last, I would like to thank Emma for bearing with me during times of frustration.

Bibliography

Banks, P. M. and G. Kockarts (1973). *Aeronomy*. New York: Academic Press Inc.

Bowles, K. L. (1958, December). Observation of vertical-incidence scatter from the ionosphere at 41 Mc/sec. *Phys. Rev. Lett. 1*(12), 454–455.

Brändström, U. and Å. Steen (1994). ALIS - a new ground-based facility for auroral imaging in northern Scandinavia. In *Proceedings of ESA Symposium on European Rocket and Balloon Programmes*, Number ESA SP-355. Eurpean Space Agency.

Carlson, C. W., R. F. Pfaff, and J. G. Watzin (1998). The Fast Auroral SnapshoT (FAST) mission. *Geophys. Res. Lett. 25*(12), 2013–2016.

Dougherty, J. P. and D. T. Farley (1960). A theory of incoherent scattering of radio waves by a plasma. *Proc. Roy. Soc. London A, 259*, 79–99.

Dougherty, J. P. and D. T. Farley (1963). A theory of incoherent scattering of radio waves by a plasma: 3. Scattering in a partly ionized gas. *J. Geophys. Res. 68*(19), 5473–5486.

Farley, D. T. (1966). A theory of incoherent scattering of radio waves by a plasma: 4. The effect of unequal ion and electron temperatures. *J. Geophys. Res. 71*(17), 4091–4098.

Farley, D. T., J. P. Dougherty, and D. W. Barron (1961). A theory of incoherent scattering of radio waves by a plasma: II. Scattering in a magnetic field. *Proc. Roy. Soc. London A, 263*, 238–258.

Folkestad, K., T. Hagfors, and S. Westerlund (1983). EISCAT: An updated description of technical characteristics and operational capabilities. *Radio Sci. 18*, 867–879.

Gordon, W. E. (1958). Incoherent scattering of radio waves by free electrons with applications to space exploration by radar. *Proc. IRE 46*, 1824.

Gustavsson, B., T. Sergienko, I. Häggström, and F. Honary (2001). Simulation of high energy tail of electron distribution function. Submitted to Adv. Space Res.

Häggström, I., M. Hedin, T. Aso, A. Pellinen-Wannberg, and A. Westman (2000). Auroral field-aligned currents by incoherent scatter plasma line observations in the E region. *Adv. Polar Upper Atmos. Res. 14*, 103–121. arXiv:physics.space-ph/0003019.

Hedin, M. and I. Häggström (2002). Incoherent scatter spectra for non-Maxwellian plasmas. Will appear in Proceeding from Radiovetenskap och Kommunikation 02.

Hedin, M., I. Häggström, A. Pellinen-Wannberg, L. Andersson, U. Brändström, B. Gustavsson, Å. Steen, A. Westman, G. Wannberg, T. van Eyken, T. Aso, C. Cattell, C. W. Carlson, and D. Klumpar (2000). 3-D extent of the main ionospheric trough—a case study. *Adv. Polar Upper Atmos. Res.* (14), 157–162. arXiv:physics.space-ph/0001043.

Jackson, J. D. (1975). *Classical Electrodynamics* (2 ed.). John Wiley and Sons, Inc.

Kivelson, M. G. and C. T. Russell (Eds.) (1995). *Introduction to Space Physics*. Cambridge University Press.

Lehtinen, M. and I. Häggström (1987). A new modulation principle for incoherent scatter measurements. *Radio Sci. 22*, 625–634.

Lehtinen, M. S. (1986). *Statistical theory of incoherent scatter radar measurments*. Ph. D. thesis, Finnish Metrological Institute. EISCAT Technical Note 86/45.

Nyquist, H. (1928, July). Thermal agitation of electric charge in conductors. *Phys. Rev. 32*, 110–113.

Rees, M. H. (1963). Auroral ionization and excitation by incident energetic electrons. *Planet. Space Sci. 11*, 1209–1218.

Swartz, W. E. and D. T. Farley (1979). A theory of incoherent scattering of radio waves by a plasma: 5. The use of the Nyquist theorem in general quasi-equilibrium situations. *J. Geophys. Res. 84*(A5), 1930–1932.

Wannberg, G., I. Wolf, L.-G. Vanhainen, K. Koskenniemi, J. Röttger, M. Postila, J. Markkanen, R. Jacobsen, A. Stenberg, R. Larsen, S. Eliassen, S. Heck, and A. Huuskonen (1997). The EISCAT Svalbard radar: A case study in modern incoherent scatter radar system design. *Radio Sci. 32*(6), 2283–2307.

Paper I

3-D extent of the main ionospheric trough—a case study

Mikael Hedin, Ingemar Häggström, Asta Pellinen-Wannberg, Laila Andersson, Urban Brändström, Björn Gustavsson, Åke Steen, Assar Westman, Gudmund Wannberg, Tony van Eyken, Takehiko Aso, Cynthia Cattell, Charles W. Carlson and Dave Klumpar

Adv. Polar Upper Atmos. Res. (14) 157–162, 2000

Typeset in single column by the author

3-D extent of the main ionospheric trough —a case study

Mikael Hedin[1], **Ingemar Häggström**[1], **Asta Pellinen-Wannberg**[1], **Laila Andersson**[1], **Urban Brändström**[1], **Björn Gustavsson**[1], **Åke Steen**[1], **Assar Westman**[2], **Gudmund Wannberg**[2], **Tony van Eyken**[3], **Takehiko Aso**[4], **Cynthia Cattell**[5], **Dave Klumpar**[6] **and Charles W. Carlson**[7]

[1]Swedish Institute of Space Physics, Box 812, S-981 28 Kiruna, Sweden.
[2]EISCAT Scientific Association, Box 812, S-981 28 Kiruna, Sweden.
[3]EISCAT Scientific Association, Postboks 432, N-9170 Longyearbyen, Norway.
[4]National Institute of Polar Research, 1-9-10 Kaga, Itabashi-ku, Tokyo 173, Japan.
[5]School of Phys. and Astr., Univ. of Minnesota, MN 55455, USA.
[6]Space Sciences Laboratory, Univ. of California, Berkeley, CA 94720, USA.
[7]Lockheed-Martin Palo Alto Research Labs, CA 94304, USA.

Abstract

The EISCAT radar system has been used for the first time in a four-beam meridional mode. The FAST satellite and ALIS imaging system is used in conjunction to support the radar data, which was used to identify a main ionospheric trough. With this large latitude coverage the trough was passed in $2\frac{1}{2}$ hours period. Its 3-dimensional structure is investigated and discussed. It is found that the shape is curved along the auroral oval, and that the trough is wider closer to the midnight sector. The position of the trough coincide rather well with various statistical models and this trough is found to be a typical one.

1 Introduction

The main ionospheric trough is a typical feature of the sub-auroral ionospheric F-region, where it is manifest as a substantial depletion in electron concentration. It is frequently observed in the nighttime sector, just equatorward of the auroral zone. This trough is often referred to as the "main ionospheric trough" or "mid-latitude trough" to distinguish from troughs in other locations. The polar edge of the trough is co-located with the auroral zone. The equatorward boundary is less distinct, consisting of a gradually increasing amount of electrons, towards the plamasphere, which could be called the normal ionosphere. Inside the trough, there are electric fields present, giving rise to westward ion convection. Extensive reviews of modelling and observations of the main ionospheric trough are given by Moffett and Quegan (1983) and Rodger et al. (1992).

The present study was performed as a part of International Auroral Study (IAS). The goal for IAS was to provide simultaneous observations from ground and space of auroral processes. An important part of IAS was the FAST (Carlson et al., 1998) satellite. FAST was planned with significant ground-base support, *i.e.*, control station and supporting scientific instrument, in Alaska, but as all polar orbiting satellites also passes over northern Scandinavia, it is well suited for coordination with ground-based instrument there as well. The most important instrument, besides the EISCAT radars, is ALIS (Brändström and Steen, 1994), the camera network in northern Sweden for auroral imaging.

2 The 4-beam EISCAT radar configuration

Previous radar experiments have used different scanning patterns to determine the topography of the trough; Collis and Häggström (1988) used a wide latitude scan (EISCAT common program experiment CP-3), Collis and Häggström (1989) used a small 4-position scan (CP-2), and Jones et al. (1997) used a combination of a wide scan to find the trough, and a narrow scan to observe the structure. Also a single position tri-static radar mode (CP-1) has been used by Häggström and Collis (1990). These methods all give a trade-off

between time and space resolution—the more scan points the longer the time before subsequent observations of the same position, and for small and fast scans the range in space is often insufficient

Here we use for the first time all the EISCAT radars in a four-beam configuration close to the meridian plane to get a wide area of observation without losing time resolution. The EISCAT Svalbard Radar (ESR) (Wannberg et al., 1997) is field aligned (elevation 81.5°) at invariant latitude (ILAT) 75.2°N. The mainland tri-static UHF system (Folkestad et al., 1983) is also field aligned (elevation 77.4°) at ILAT 66.3°N. Between these, the Tromsø VHF radar is used in a "split-beam mode", with the eastern antenna panels pointing north (70° elevation) and the western panels pointing vertical. The data is split into two sets, VHF-N (north) and VHF-V (vertical).

The combined "meta-radar" has a huge fan-like observation area around 70°N–80°N in geographic latitude.

3 Characteristics of the observed trough

The radar observations of the trough in question are shown in figure 1. The trough is seen as the clear decrease in electron density, and we determine the time in UT for the radars passing under the trough to be 1710–1720, 1820–1900, 1845–1925 and 1900–1940 respectively. The more prominent density increase for the Tromsø sites after 2000 UT is not the edge of the trough, rather typical F-region blobs, poleward of the trough.

In figure 1 we see that the trough extends through all of the F-region, but not in the E-region. Note that white color is both highest density and no usable data, but generally no data is due to low density and this is seen to be the case here in the trough. In the northern part of the trough (later time in the data), we can actually see some typical weak ionization in the E-region, interpreted as diffuse aurora.

We compare the actual location of the trough minimum with predicted positions from models by Collis and Häggström (1988); Köhnlein and Raitt (1977); Rycroft and Burnell (1970) respectively[1]—all linear in SLT (solar local time) and Kp. For the present day, Kp values are $1-$ before and 1o after 1800 UT. In figure 2, these model values are shown together with the actual position of the whole trough as determined from ESR, FAST, VHF-N, VHF-V and UHF respectively (from high to low latitude). We see that the deviations from the model predictions are substantial, and conclude that the linear models are not adequate for use over a wide range in latitude and time. This is not surprising because the fits used to construct the equations all had a big spread, even though the correlations were quite good.

A more recent study based on satellite data is made by Karpachev et al. (1996), where they use both latitude and longitude to make a statistical model not restricted to linear relations. In this model, the time used is magnetic local time (MLT), which is reasonable because the trough structure is governed by the earth magnetic field. They use both linear and non-linear time dependency, and find that for midnight hours, the difference is rather small, compared to the large spread in the data, but favours the non-linear time dependency.

From the start time of when each radar beam enters the trough, as seen in figure 1, we can estimate the trough apparent southward speed to be around 12 km/min from Longyearbyen to Tromsø, and around 4 km/min between the Tromsø beams. Assuming that the trough appears to pass over ESR and between the mainland radars with the respective speed, we can make a crude estimate of the vertical shape of the trough and the width: From the plot in figure 1, we estimate that the southward (early) wall, taken as the border of blue and green color, has an inclination of 35° for the VHF-N beam and 21° for VHF-V. This should be compared with the direction of the magnetic field at Tromsø, zenith angle 13° southwards. If we assume the trough wall to be field aligned, the anticipated inclination is 33° (20+13) for VHF-N and 13° for VHF-V, in good agreement with the rough estimate. In the plot of the field aligned beams, ESR and UHF, the trough wall appears vertical, which means it is field-aligned. The passing time for Longyearbyen is

[1] with Rycroft and Burnell (1970) changed to invariant latitude as suggested by Köhnlein and Raitt (1977)

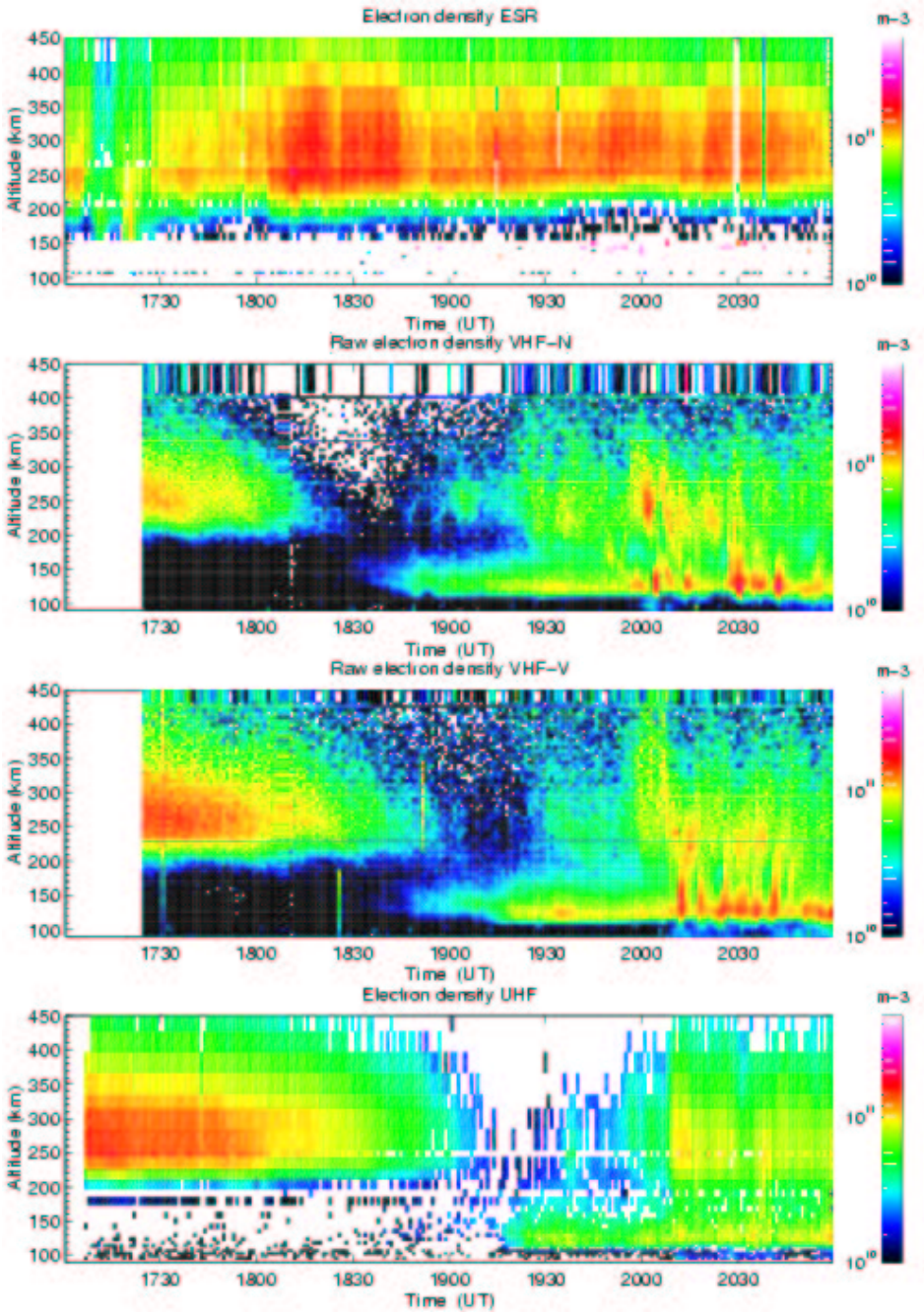

Fig. 1. EISCAT electron density (ESR and UHF) and raw electron density (VHF-N and VHF-V) plots for 970314. The electron concentration (in m^{-3}) is colour coded, with UT on horizontal and height (km) on vertical axis.

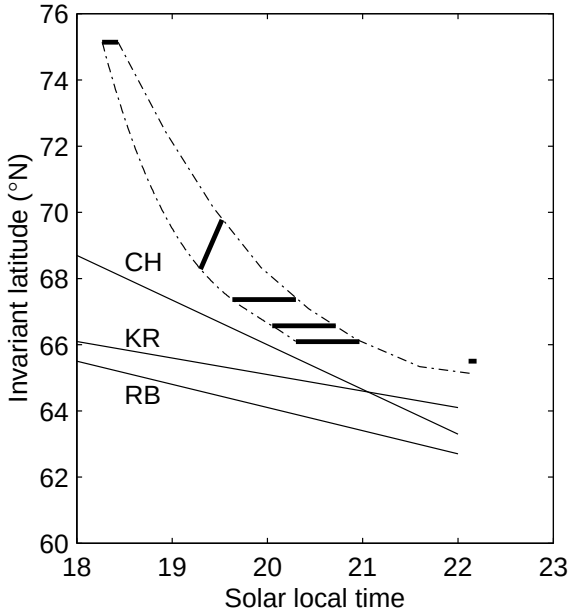

Fig. 2. The thick lines show the coordinates in ILAT and SLT (solar local time) of the actual pass of the trough as determined from (high to low latitude) ESR, FAST, VHF-N, VHF-V and UHF. The dash-dotted line is an estimate of the trough boundaries, extrapolated to later time from these direct measurements. The diffuse aurora observed with ALIS is indicated by the small spot in the latest part of the plot, just above the border of the estimated trough boundary. The solid lines show predictions for location of trough minima from models discussed in the text.

10 minutes, which, using the above speeds, gives a width of 120 km, and for the Tromsø beams the time is 40 minutes, which gives a width of 160 km, both in north-south direction. This assumes the trough to consist of two straight parts, one extending from over Longyearbyen and Tromsø, the other over the Tromsø beams, instead of the actual arc-like shape as seen in figure 2, but it will anyway give an indication of the size. The east-west size can be estimated by using the earth rotation, this gives a velocity of 6.1 km/min, and a size of 61 km for Longyearbyen and around 10 km/min with size 400 km over Tromsø. The actual width, measured perpendicular over the trough extent is then 54 km for the part passing over Longyearbyen and 149 km for the part passing over Tromsø. That is, the trough radial width is actually broader equatorwards, closer to magnetic midnight. This is shown in figure 2.

The FAST satellite does not carry sounding instruments, so trough signatures are not as obvious to detect. The signature used is the precipitation north of the trough and the electric field associated with the ion ($E \times B$) drift (absent south of the trough). It is known from earlier studies (Collis and Häggström, 1988) that there is a westward ion convection in the trough, which is absent outside. The satellite passes over the trough 1742–1743 UT as shown in figure 2.

During the night, the auroral imaging system ALIS was not operating continuously because there was no significant aurora and it was partly cloudy. However, some pictures were taken at relevant times, and they show faint diffuse aurora around the time when ALIS passes under the trough poleward boundary. If we plot the position of diffuse aurora from ALIS, it located just in the northern part of the trough region as extrapolated from the other more direct measurements in figure 2.

If we compare the observed trough with the relevant typical features of the mid-latitude trough as described in Moffett and Quegan (1983), we can say that the present trough is quite typical.

4 Conclusions

The EISCAT facility has been used in a new four-beam meridional mode. The ESR and UHF system are field-aligned, and the VHF system is split in two beams in between. This gives a very wide latitude range for observation, well suited to study ionospheric structures moving over large range in short time. With this configuration, no time resolution is lost.

In this case, the main ionospheric trough has been observed as high as 75°N ILAT down to 66°N ILAT. The observed trough is a quite typical one–it has all the common features known from earlier studies. The present observation is made when the Kp index was low and stable, and so the trough was also quite non-dramatic, but this means that the trough is rather stationary over the big area of observation. This rules out significant time variations of the trough position, as would have been the case in a more active environment, enabling investigation over a relatively long period as the earth moves under it.

If we calculate the apparent southward motion of the trough, the speed is over 10 km/min between Longyearbyen and Tromsø, but about 4 km/min between the Tromsø sites. This is consistent if the trough is really an oval shape, so that Longyearbyen passes under it close to perpendicular, but for Tromsø latitudes the direction of passage is much more oblique, thereby the apparent southward motion is much slower. The trough is also seen to be wider towards magnetic midnight. The earlier proposed linear equations for trough motions are shown not to be valid over the latitude range in question.

Coordinated studies poses substantial difficulties, most of which are not scientific but rather administrative or probabilistic by nature. Nevertheless, if one measurement (EISCAT in this case) is good, the others can often be used to extract some extra information in support.

Acknowledgement. We gratefully acknowledge assistance of the EISCAT staff. The EISCAT Scientific Association is supported by France (CNRS), Germany (MPG), United Kingdom (PPARC), Norway (NFR),Sweden (NFR), Finland (SA) and Japan(NIPR).

References

Brändström, U. and Steen, Å., ALIS - a new ground-based facility for auroral imaging in northern scandinavia, in *Proceedings of ESA Symposium on European Rocke and Balloon Programmes*, ESA SP-355, ESA, 1994.

Carlson, C. W., Pfaff, R. F., and Watzin, J. G., The fast auroral snapshot mission, *Geophys. Res. Lett.*, *25*, 2013–2016, 1998.

Collis, P. N. and Häggström, I., Plasma convection and auroral precipitation processes associated with the main ionospheric trough at high latitudes, *J. Atmos. Terr. Phys.*, *50*, 389–404, 1988.

Collis, P. N. and Häggström, I., High resolution measurements of the main ionospheric trough using EISCAT, *Adv. Space Res.*, *9*, 545–548, 1989.

Folkestad, K., Hagfors, T., and Westerlund, S., EISCAT: An updated description of technical characteristics and operational capabilities, *Radio Sci.*, *18*, 867–879, 1983.

Häggström, I. and Collis, P., Ion composition changes during F-region density depletions in the presence of electric fields at auroral latitudes, *J. Atmos. Terr. Phys.*, *52*, 519–529, 1990.

Jones, D. G., Walker, I. K., and Kersley, L., Structure of the polward wall of the trough and the inclination of the geomagnetic field above the EISCAT radar, *Ann. Geophys.*, *15*, 740–746, 1997.

Karpachev, A. T., Deminov, M. G., and Afonin, V. V., Model of the mid-latitude ionospheric trough on the base of cosmos-900 and intercosmos-19 satellites data, *Adv. Space Res.*, *18*, 6221–6230, 1996.

Köhnlein, W. and Raitt, W. J., Position of the mid-latitude trough in the topside ionosphere as deduced from ESRO 4 observations, *Planet. Space Sci.*, *25*, 600–602, 1977.

Moffett, R. J. and Quegan, S., The mid-latitude trough in the electron concentration of the ionospheric F-layer: a review of observations and modeling, *J. Atmos. Terr. Phys.*, *45*, 315–343, 1983.

Rodger, A. S., Moffett, R. J., and Quegan, S., The role of ion drift in the formation of ionisation troughs in the mid- and high-latitude ionosphere—a review, *J. Atmos. Terr. Phys.*, *54*, 1–30, 1992.

Rycroft, M. J. and Burnell, S. J., Statistical analysis of movement of the ionospheric trough and the plasmapause, *J. Geophys. Res.*, *75*, 5600–5604, 1970.

Wannberg, G., Wolf, I., Vanhainen, L.-G., Koskenniemi, K., Röttger, J., Postila, M., Markkanen, J., Jacobsen, R., Stenberg, A., Larsen, R., Eliassen, S., Heck, S., and Huuskonen, A., The EISCAT Svalbard radar: A case study in modern incoherent scatter radar system design, *Radio Sci.*, *32*, 2283–2307, 1997.

Paper II

Auroral field-aligned currents by incoherent scatter plasma line observations in the E region

Ingemar Häggström, Mikael Hedin, Takehiko Aso, Asta Pellinen-Wannberg and Assar Westman

Adv. Polar Upper Atmos. Res. (14) 103–121, 2000

Typeset in single column by the author

Auroral field-aligned currents by incoherent scatter plasma line observations in the E region

Ingemar Häggström[1,2], **Mikael Hedin**[2], **Takehiko Aso**[1], **Asta Pellinen-Wannberg**[2] **and Assar Westman**[2]

[1]National Institute of Polar Research, 1-9-10 Kaga, Itabashi-ku, Tokyo 173-8515, Japan.
[2]Swedish Institute of Space Physics, Box 812, S-981 28 Kiruna, Sweden.

Abstract

The aim of the Swedish-Japanese EISCAT campaign in February 1999 was to measure the ionospheric parameters inside and outside the auroral arcs. The ion line radar experiment was optimised to probe the E-region and lower F-region with as high a speed as possible. Two extra channels were used for the plasma line measurements covering the same altitudes, giving a total of 3 upshifted and 3 downshifted frequency bands of 25 kHz each. For most of the time the shifted channels were tuned to 3 (both), 4 (up), 5.5 (down) and 6.5 (both) MHz.

Weak plasma line signals are seen whenever the radar is probing the diffuse aurora, corresponding to the relatively low plasma frequencies. At times when auroral arcs pass the radar beam, significant increases in return power are observed. Many cases with simultaneously up and down shifted plasma lines are recorded. In spite of the rather active environment, the highly optimised measurements enable investigation of the properties of the plasma lines.

A modified theoretical incoherent scatter spectrum is used to explain the measurements. The general trend is an upgoing field-aligned suprathermal current in the diffuse aurora, There are also cases with strong suprathermal currents indicated by large differences in signal strength between up- and downshifted plasma lines. A full fit of the combined ion and plasma line spektra resulted in suprathermal electron distributions consistent with models.

1 Introduction

The incoherent scatter spectrum consists mainly of two lines, the widely used and relatively strong ion line and the very weak easily forgotten broadband electron line. There is also another line present, the plasma line, due to scattering from high frequency electron waves, namely Langmuir waves. From the downgoing and upgoing Langmuir waves, two plasma lines can be detected by the radar. The frequency shift from the transmitted signal is the frequency of the scattered Langmuir wave plus the Doppler shift caused by electron drift. Plasma lines can be used to measure the electron drift and hence the line-of-sight electric current. The problem in ion line analysis with the uncertainty of the radar constant can be solved by the plasma line frequency determination and when that is done the speed of measurement can be significantly increased by including the plasma line in the ion line analysis. However, since the frequency of the plasma lines is not known beforehand, and the frequency is varying with height, it is difficult to measure them with enough resolution.

There have been a number of reports on plasma line measurements and their interpretation. Most of them have discussed the frequency shift from the transmitted pulse and the scattering has mainly been from the F-region peak, e.g. Showen (1979), Kofman et al. (1993) and Nilsson et al. (1996a). The latter two showed also that the simple formula for the Langmuir wave frequency,

$$f^2 = f_p^2(1 + 3k^2\lambda_D^2) + f_c^2 \sin^2 \alpha \tag{1}$$

where f_p is the plasma frequency, k the wave number f_c the electron gyro frequency, λ_D the electron Debye length and α the angle between the scattering wave and

the magnetic field, is valid to within a few kHz and thus enough to set the radar system constant. To be able to deduce any electron drifts, or current, out of the positions of the lines these authors also show that Eq. (1) is not sufficient, and it is necessary to carry out more accurate calculations. Hagfors and Lehtinen (1981) had also to go to further expansions in deriving the ambient electron temperature from the plasma lines. The fact that so many reports deal with the F region peak is due to the altitude profile shape of the plasma line frequency, which according to Eq. (1) will also show a peak around that height. The measurements can thus be made relatively easily using rather coarse height resolution but good frequency resolution and only detect the peak frequency. Measurements using the same strategy, but at other heights, have been made with a chirped radar by matching the plasma line frequency height gradient and the transmitter frequency gradient (Birkmayer and Hagfors, 1986; Isham and Hagfors, 1993). This technique allows determination of the Langmuir frequency with very high frequency resolution, but do not use the radar optimally, since the chirped pulse cannot be used for anything else than plasma line measurements.

The enhancement of the plasma lines, which occurs in the presence of suprathermal electron fluxes (Perkins and Salpeter, 1965), either photoelectrons or secondaries from auroral electrons, has been investigated by Nilsson et al. (1996b), where they also calculate predictions of plasma line strength for different incoherent scatter radars and altitudes. They also show that the power of the plasma line is rather structured with respect to ambient electron density, depending on fine structure in the suprathermal distributions due to excitations of different atmospheric constituents.

Incoherent scatter plasma lines in aurora are more difficult to measure since the variations in the plasma parameters are strong with large time and spatial gradients. Reports of auroral plasma lines in the aurora are also more rare, and most of them are based on too coarse time resolution (Wickwar, 1978; Kofman and Wickwar, 1980; Oran et al., 1981; Valladares et al., 1988), with resolutions ranging from 30 seconds up to 20 minutes. The enhancements over the thermal level were high, but consistent with what could be expected of model calculations of suprathermal electron flux. They also tried to calculate currents and electron temperature from the frequency shifts of the plasma lines but with very large error bars. Kirkwood et al. (1995) used the EISCAT radar and the filter bank technique and recorded much higher intensities of the plasma lines, since they got down to resolutions of 10 seconds, and showed also that the plasma-turbulence model proposed by Mishin and Schlegel (1994) was not consistent with the data, but could be explained by reasonable fluxes of suprathermal electrons.

In this paper we present data obtained with the high resolution alternating code technique (Lehtinen and Häggström, 1987), as was also done for F-region plasma lines by Guio et al. (1996), with even higher intensities due to the time resolutions of 5 seconds. An interesting, but at the time of the experiment not realisable at EISCAT, technique would have been the type of coded long pulses used by Sulzer and Fejer (1994) for HF-induced plasma lines. From relative strengths between up- and downshifted lines we detect a general trend of upgoing field-aligned currents in the diffuse aurora carried by the suprathermal electrons. We propose a generalisation of the theoretical incoherent scatter spectrum, to include multiple shifted electron distributions, and in one example we do a full 7-parameter fit of the incoherent scatter spectrum, including the enhanced plasma lines assuming Maxwellian secondary electrons, resulting in the first radar measurement of its flux and a current carried by the thermal electrons.

2 Experiment

The measurements we present were collected by the 930 MHz EISCAT UHF incoherent scatter radar, with its transmitter located at Ramfjordmoen in Norway

(69.6 °N, 19.2 °E, L=6.2). The signals scattered from the ionosphere were received at stations in Kiruna, Sweden and Sodankylä, Finland as well as at the transmitting site. General descriptions of the radar facility are given by Folkestad et al. (1983) and Baron (1984). Local magnetic midnight at Ramfjordmoen is at about 2130 UT. The aim, in the Swedish-Japanese EISCAT campaign in February 1999, was to measure the ionospheric parameters inside and outside the auroral arcs.

For this a 3 channel ion line alternating code (Lehtinen and Häggström, 1987) experiment, optimised to probe the E-region and lower F-region with as high a speed as possible, was developed. The 16 bit strong condition alternating code with bitlengths of 22 μs was used, giving 3 km range resolution, and with a sample rate of 11 μs the range separations in consecutive spectra were 1.65 km. Fig. 1 shows the transmission/reception scheme of the first 20 ms of the radar cycle. The whole alternating code sequence takes about 0.3 s to complete. During this period the incoherent scatter autocorrelation functions (ACF) at the probed heights should not change significantly for the alternating codes to work. In order to keep this as short as possible, the short pulses, normally used for zerolag estimation, were dropped and instead a pseudo zero lag, obtained from decoding the power profiles of the different codes in the alternating code sequence, was used. Fig. 2 shows the range-lag ambiguity function for this lag centred around 0 μs in the lag direction, but the main contribution to the signal comes from around 7 μs. The more normal lag centred at 22 μs is also shown for comparison. The range extents are rather similar but the power is, of course, considerably lower for the pseudo zero lag. Nevertheless, this is taken care of in the analysis and this lag is rather important in events with high temperatures giving broad ion line spectra or narrow ACFs. The transmitting frequencies were chosen to give maximum radiated power for a given high voltage setting.

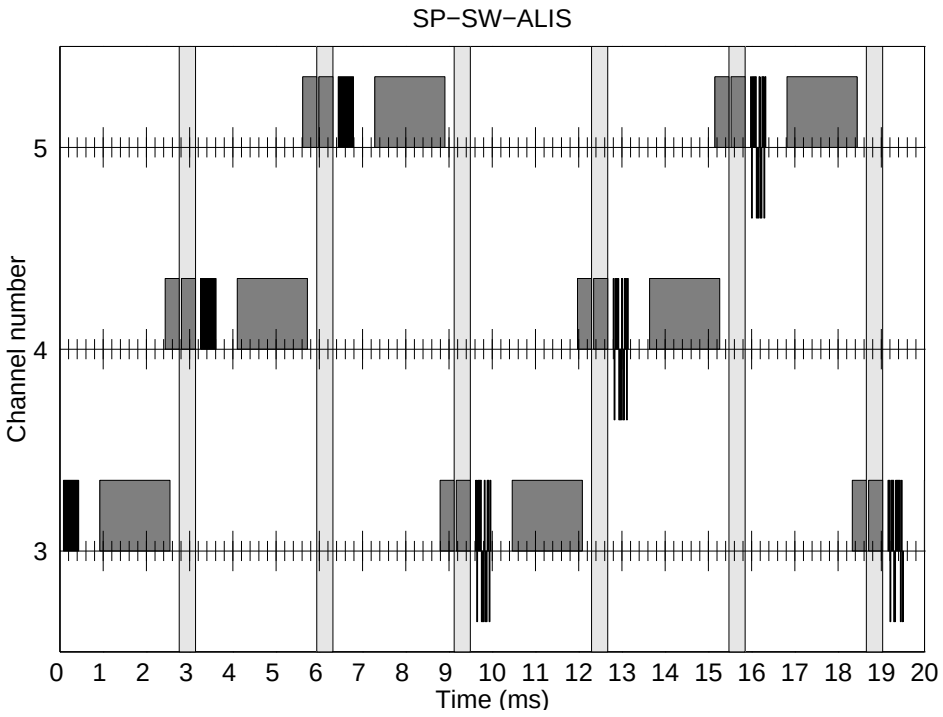

Fig. 1. Transmission (black) and reception (dark gray) scheme for part of SP-SW-ALIS. A 16-bit alternating code, 22 μs bits, is cycled over 3 frequencies. The interscan period is 9 ms and the total cycle takes 300 ms. The plasma line channels were set to sample the same range extent as the ion lines.

The monostatic plasma line part of the experiment used two channels covering

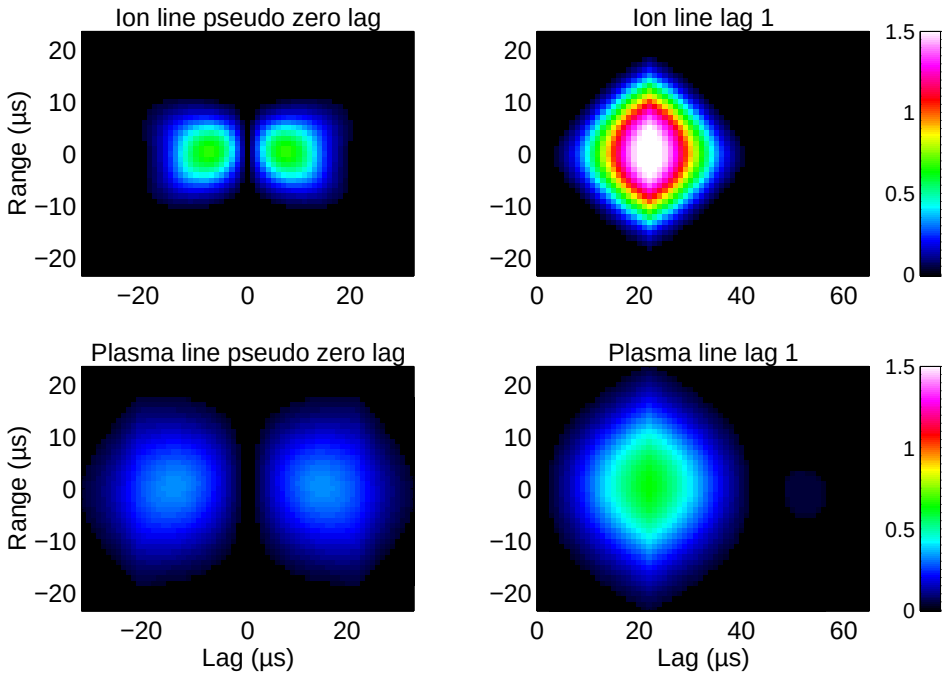

Fig. 2. Range-lag ambiguity function for the first two lags, a) ion line and b) plasma line. The range, given in μs, can be converted to km with multiplication of 0.15. The differences between the ion and plasma line ambiguity functions are due to the use of different receiver filters.

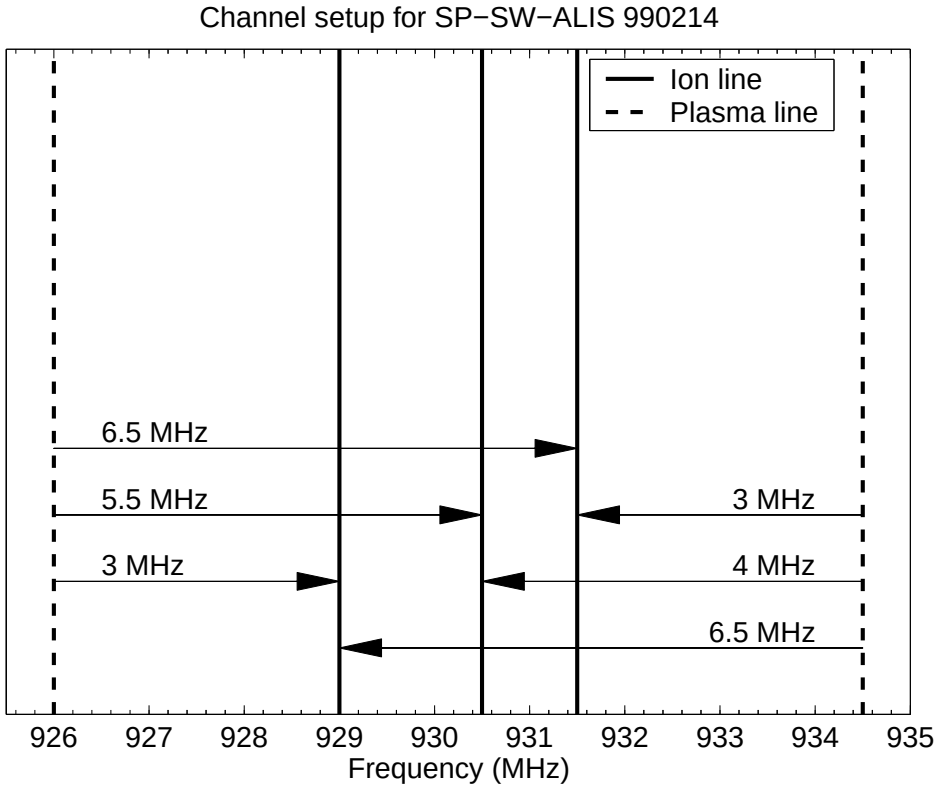

Fig. 3. The frequency setup for the experiment. The plasma line channels were fixed to 926 and 934.5 MHz, giving "simultaneously" up and downshifted frequencies at 3 and 6.5 MHz. In addition there is an upshifted line at 4 and a downshifted at 5.5 MHz.

the same ranges as the ion line but with 3.3 km range separations between the spectra. The frequency setup for the experiment, illustrated in Fig. 3, gives the possibility for 3 upshifted and 3 downshifted bands. For 3 MHz and 6.5 MHz frequency shifts, both the up- and downshifted plasma lines were measured. In addition there was a 4 MHz upshifted and a 5.5 MHz downshifted band. The width of these bands should have been set to match the bit length of the codes used, 50 kHz, but unfortunately this was not the case and 25 kHz wide filters were erroneously used. This gave naturally less signal throughput, and in Fig. 2 the corresponding range/lag ambiguity functions for the plasma line channels are included for the first two lags. The decoding still works, giving just slightly increased unwanted ambiguities, but above all the pseudo zero lag is moved out to a larger lag value. This fact, with one exception, almost ruled out the possibilities to measure plasma line spectra because, as will be shown here later, they are likely to be rather wide, due to large time and height gradients of the plasma parameters. This lead the analysis to use mainly the undecoded zerolag, which after integration over the different codes, almost resembles the shape of a 352 μs (16×22 μs) long pulse.

The experiment contained a large number of antenna pointings in order to follow the auroral arcs, but as this day was cloudy over northern Scandinavia the transmitting antenna was kept fixed along the local geomagnetic field line. The remote sites, receiving only ion lines, were monitoring the same pulses as the transmitting site, and were used to measure the drifts in the F-region, to derive the electric field. Thus, these antennas intersected the transmitted beam at the F-region altitude giving the best signal, for this day mostly at 170 km.

3 Measurements

3.1 Ion line

The experiment started at 1900 UT on 14 February 1999 and continued until 2300 UT. Fig. 4 shows an overview of the parameters deduced from the ion line measurements, which were analysed using the on-line integration time, 5 seconds, in order to be compared to the plasma line data. The analysis was done using the GUISDAP package (Lehtinen and Huuskonen, 1996), but a correction of 45% of the radar system constant used in the package had to be invoked to fit the plasma line measurements according to Eq. (1). This short integration time was possible due to the highly optimised mode used, with all the transmitter power concentrated to the E-region. In range, some integration was done, so that at lower heights 2 range gates were added together and with increasing height the number of gates added together increases to 15 in the F-region.

There is a rather strong E-region from the start, but no real arcs, and we interpret this as diffuse aurora. The peak electron density shows some variation, but as time goes the E-region ionisation decreases until 2050 UT, where it is almost gone. The density peak during this time was at around 120 km altitude and the lower edge of the E-region at 110 km, but at times the ionisation reaches down to 100 km. At 2050 UT and onwards until 2240 UT the ionosphere above Tromsø became more active and several auroral arcs passed the beam. Around some of the arcs there are short-lived enhancements of electric field, seen as F-region ion and E-region electron temperature increases. In the last 10 minutes of the experiment the arc activity disappeared and again there was diffuse aurora. From the field aligned ion drifts it is evident that there is a rather strong wave activity in the diffuse aurora until 2050 UT, while it is not so clear in the continuation of the experiment. The last panel with the inferred electron density from the pseudo zero lag shows the same features as the fitted density panel but with highest possible resolution since no height integration is made.

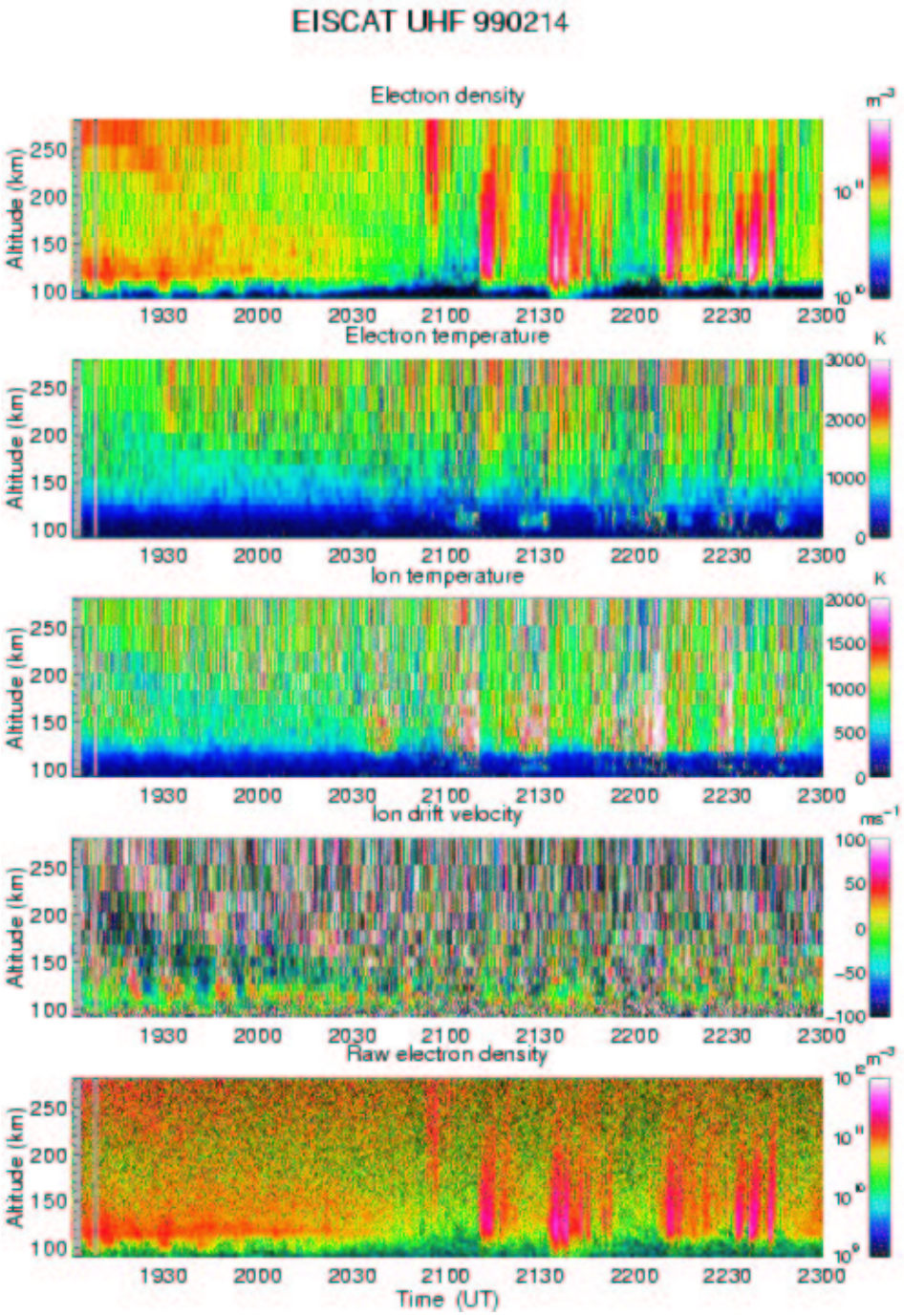

Fig. 4. Summary of results from the ion line experiment. All panels shows the parameters in a altitude versus time fashion with the antenna directed along the geomagnetic field line. Panels from top: Electron density, electron temperature, ion temperature, line-of-sight ion drift velocity and electron density based on only the returned power. The data were analysed with 5 s integration due to the active conditions.

3.2 Plasma line

Since the analysis of the plasma lines was forced to handle the undecoded zerolags of the alternating codes, it was necessary to analyse their profile shape. Fig. 5 shows how this analysis was performed. From the fitted parameters of the ion line, electron density and temperature, a profile of the approximate Langmuir frequency can be calculated using Eq. (1). When probing at fixed frequency, there will be scattered signal only from heights where the probing and Langmuir frequencies match each other. The effect of the undecoded zerolag is similar to the one where a normal long pulse is used, but with a lower signal strength. So, the profile shape will be a square pulse centred on the corresponding altitude, since no gating is performed. Because the signal strengths are rather weak compared to the system temperature, there is a great deal of noise in the profile shape. To be able to extract the altitude and signal power, a fitting procedure need to be performed. For this a continous function and a good first guess is needed and the measured plasma line profile was convolved with the pulse shape to have a triangular shape and also showing a peak close to the matching height.

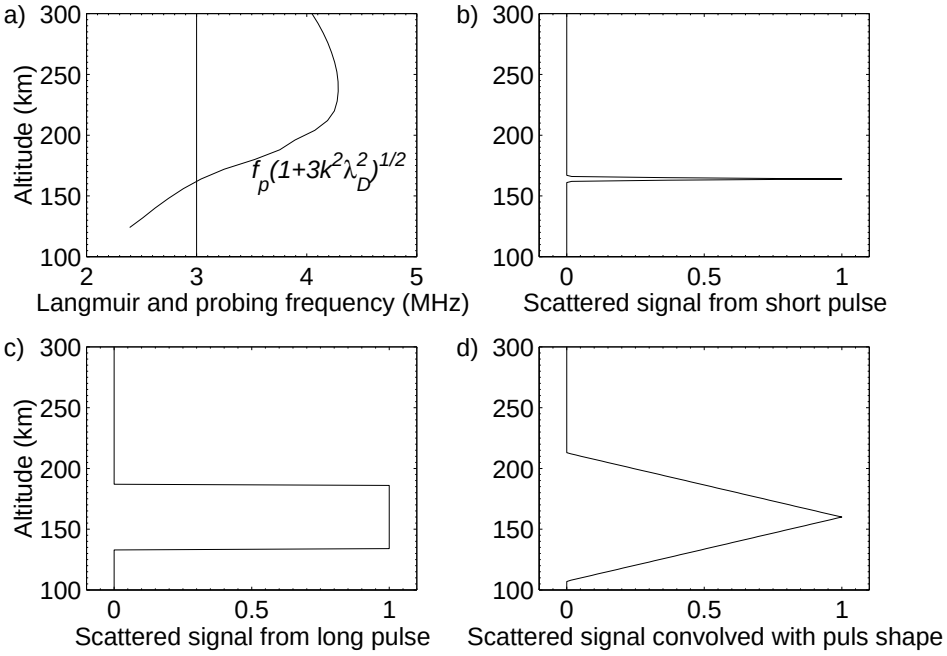

Fig. 5. Description of the analysis procedure. a) Langmuir frequency profile together with the probing frequency of 3 MHz shift. b) The echo profile using a short pulse. c) The echo profile using a long pulse. d) The echo profile of a long pulse convolved with the pulse shape.

The plasma line part of the experiment is overviewed in Fig. 6. The signal strengths shown should be compared with the UHF system temperature of about 90 K. At first glance there is almost nothing in the upshifted part, but a more careful look shows weak signals between 1940 and 2030 UT and after 2250 UT, corresponding to the occurrence of diffuse aurora. Similar echoes can also be seen in the downshifted channel, and are due to plasma lines at 3 MHz offset from the transmitted frequencies, according to the ion line measurements. In the downshifted part after 2100 UT, frequent events of rather strong signals in phase with auroral arcs pass the beam. Most of these are from the 5.5 MHz shift, but some of them also are due to plasma lines at 6.5 MHz. Such events are less frequent and for most of them there are also signals in the upshifted part.

Due to the fact that the same channel is used for several frequencies, there can be several altitudes that fulfill the matching condition between Langmuir and

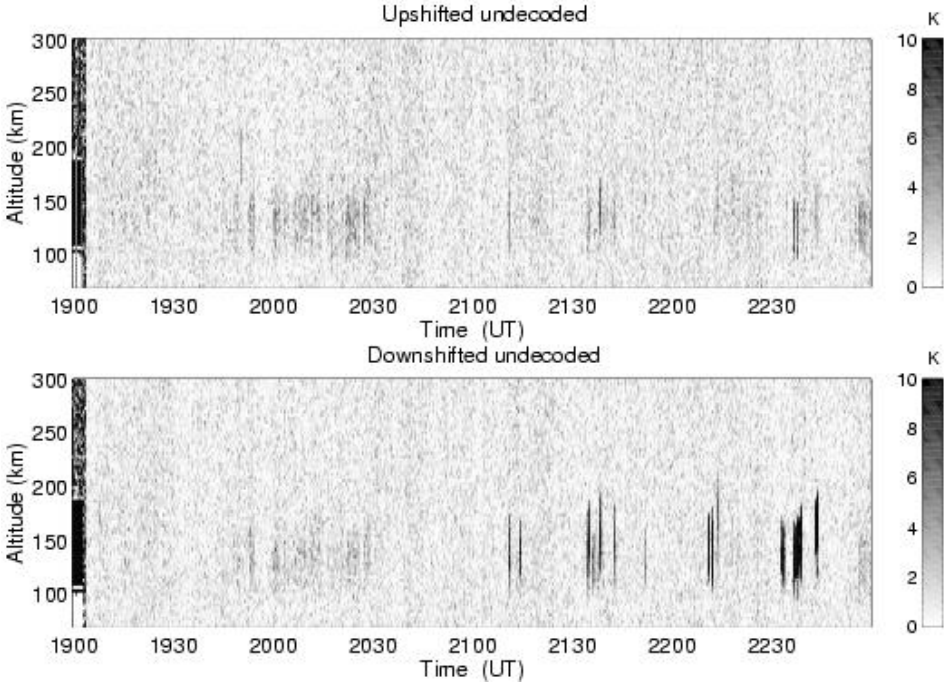

Fig. 6. Overview of the plasma line measurements. The panels show the undecoded upshifted (top panel) and downshifted returns, given as signal strengths in Kelvin.

probing frequency. This complicates the analysis somewhat, and there have to be several fits with different numbers of triangles superposed on each other. Some examples of this analysis are shown in Fig. 7, from only one plasma line to several both up- and downshifted lines. Using a lower limit of 2 K signal power, the total number of 5 second integration events with enhanced plasma lines for this evening was 256, and a total of 468 plasma line echoes were detected, divided into 220 on 3 MHz, 19 on 4 MHz, 157 on 5.5 MHz and 72 on 6.5 MHz.

4 Theory

In order to relate the plasma line measurements to physical quantities it is necessary to investigate the spectrum of the incoherent scatter process. The Nyquist theorem approach, derived in a long series of papers by Dougherty and Farley (1960, 1963), Farley et al. (1961), Farley (1966) and finally Swartz and Farley (1979), arrives at

$$\sigma(\omega) = \frac{N_e r_e^2 \sin^2\delta}{\pi} \cdot \frac{|y_e|^2 \sum_i \frac{\eta_i \Re(y_i)}{\omega - \boldsymbol{k}\cdot\boldsymbol{v}_i} + \left|jk^2\lambda_D^2 + \sum_i \mu_i y_i\right|^2 \frac{\Re(y_e)}{\omega - \boldsymbol{k}\cdot\boldsymbol{v}_e}}{\left|y_e + jk^2\lambda_D^2 + \sum_i \mu_i y_i\right|^2}, \qquad (2)$$

where

$$\eta_i = \frac{n_i q_i^2}{N_e e^2}, \qquad (3)$$

$$\mu_i = \frac{\eta_i T_e}{T_i}, \qquad (4)$$

and the index e stands for electrons and i for the different ion species. N and n are the densities, r_e the classical electron radius, v the bulk velocity, q the charge, e the electron charge and T the temperature. The complex normalised admittance function, y, contains most of the physics with the plasma dispersion function and have as main arguments the collision frequency and magnetic field. The same

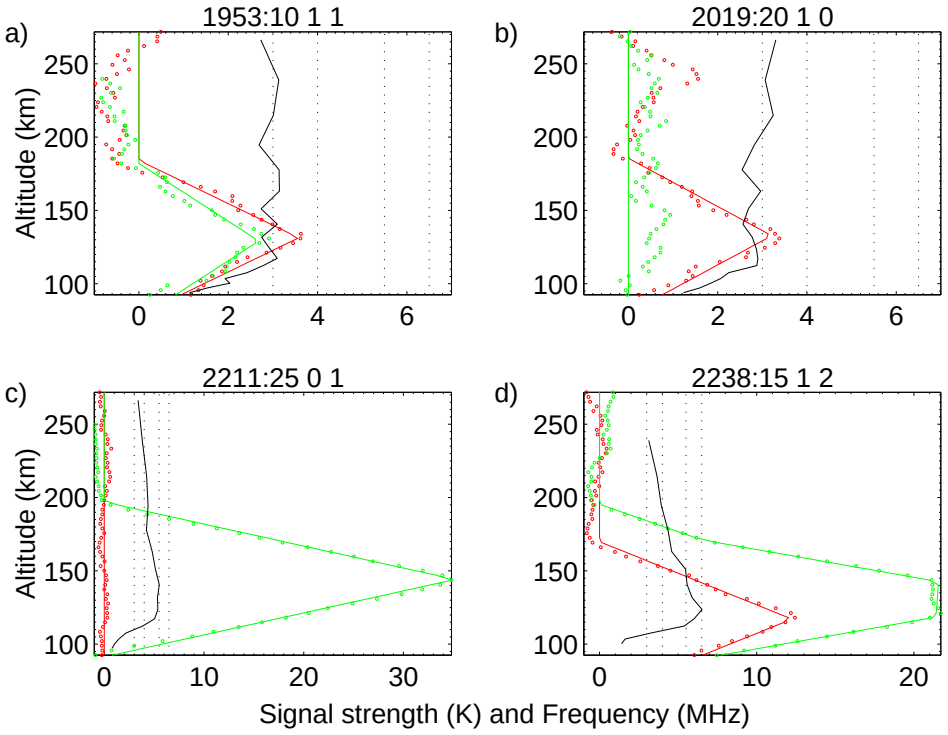

Fig. 7. Examples of measured convolved profiles (circles) and the triangle(s) fitted (lines). Included on the plots are the profiles of the Langmuir frequency (black) calculated from the parameters of ion lines fit. The value on the x-axis represent signal strength (K) and frequency (MHz) respectively. The numbers in the title shows the time of measurement and how many echoes was detected for the up- (red) and downshifted (green) frequencies. A lower limit of 2 K received signal power (2% SNR) was used. a) Simultaneous up and downshifted echoes at 3 MHz in diffuse aurora. b) An upshifted 3 MHz echo in diffuse aurora. c) A strong downshifted echo at 5.5 MHz in an auroral arc. d) Simultaneous up and downshifted echoes at 6.5 MHz and a downshifted 5.5 in an auroral arc.

result was also reached by Rosenbluth and Rostoker (1962), using the dressed particle approach. In Fig. 8 there is an example of the spectrum, showing clearly the strong ion line around zero offset frequency and the rather weak plasma lines at rather large offsets. The plasma lines become enhanced by a photo electron or auroral electron produced suprathermal electron distribution, and in order to simulate what this extra distribution does to the spectrum a modification to the formula has to be made. First, a rewriting of Eq. (2) following Swartz (1978) has to be performed in order to separate the electron and ion contributions to the spectrum:

$$S(f) = \frac{1}{\pi} \cdot \frac{\left|\frac{N_e y_e}{T_e}\right|^2 \sum_i \frac{n_i Z_i^2 \Re(y_i)}{f + k v_i/2\pi} + \left|jC_D + \sum_i \frac{n_i Z_i^2 y_i}{T_i}\right|^2 \frac{N_e \Re(y_e)}{f + k v_e/2\pi}}{\left|\frac{N_e y_e}{T_e} + jC_D + \sum_i \frac{n_i Z_i^2 y_i}{T_i}\right|^2}, \tag{5}$$

where

$$C_D = \frac{k^2 \epsilon K}{e^2}, \tag{6}$$

f is the frequency shift, $Z = q/e$, ϵ is the dielectricity and K is the Boltzmann constant. Here, a normalisation of the spectrum has also been performed, so that the zero lag of the corresponding ACF is the raw electron density and the vector velocity is replaced by the line-of-sight velocity. Using a treatment in analogy to the ion contribution, it is now possible to rewrite the spectrum to support a number of Maxwellian electron distributions as

$$S(f) = \frac{1}{\pi} \cdot \frac{\left|\sum_e \frac{N_e y_e}{T_e}\right|^2 \sum_i \frac{n_i Z_i^2 \Re(y_i)}{f + k v_i/2\pi} + \left|jC_D + \sum_i \frac{n_i Z_i^2 y_i}{T_i}\right|^2 \sum_e \frac{N_e \Re(y_e)}{f + k v_e/2\pi}}{\left|\sum_e \frac{N_e y_e}{T_e} + jC_D + \sum_i \frac{n_i Z_i^2 y_i}{T_i}\right|^2}. \tag{7}$$

In Fig. 9 the effect on the plasma lines of a suprathermal distribution with a reasonable density of 10^7 m^{-3} and width of 10 eV is shown, being lower than the ionisation energy for most ions. The plasma lines grow considerable and the integrated power over the bandwidth used in the experiment becomes comparable to the power of the ion line. It may also be noted that there is no effect at all seen in the ion line. Perkins and Salpeter (1965) have shown similar calculations, but when their method was based on large expansions to allow non-Maxwellian distributions one can here more directly superpose a few Maxwellian distributions to explain the measurements and even make fits of the spectra taken to get estimates of the suprathermal distributions, which is of great importance in auroral measurements. A consequence of Eq. (7) is that it is also possible to derive the spectrum assuming currents carried by the suprathermal distribution, since it allows different drift velocities on the various distributions. Indeed, Fig. 10, shows differential strengths on the two plasma lines, with upgoing electrons enhancing mainly the downshifted line and downgoing ones the upshifted line.

5 Discussion

Plasma line measurements in the active auroral ionosphere are not an easy task, due to the large variations in the ionospheric parameters. The Langmuir frequencies are largely dependent on the ambient electron density, making the line move considerably as the density changes, which it does on time scales of seconds. Moreover, the density height gradient makes the lines very broad when measured over a specific height interval, and at times even broader than the receiver band. A chirped radar would solve only a part of the problem at the cost of transmitter power. These complications make it hard to draw any conclusions on the power in the lines, as one does not know for sure the scattering volume or the time duration of the scattering. Bearing this in mind and to at least minimise these effects, one

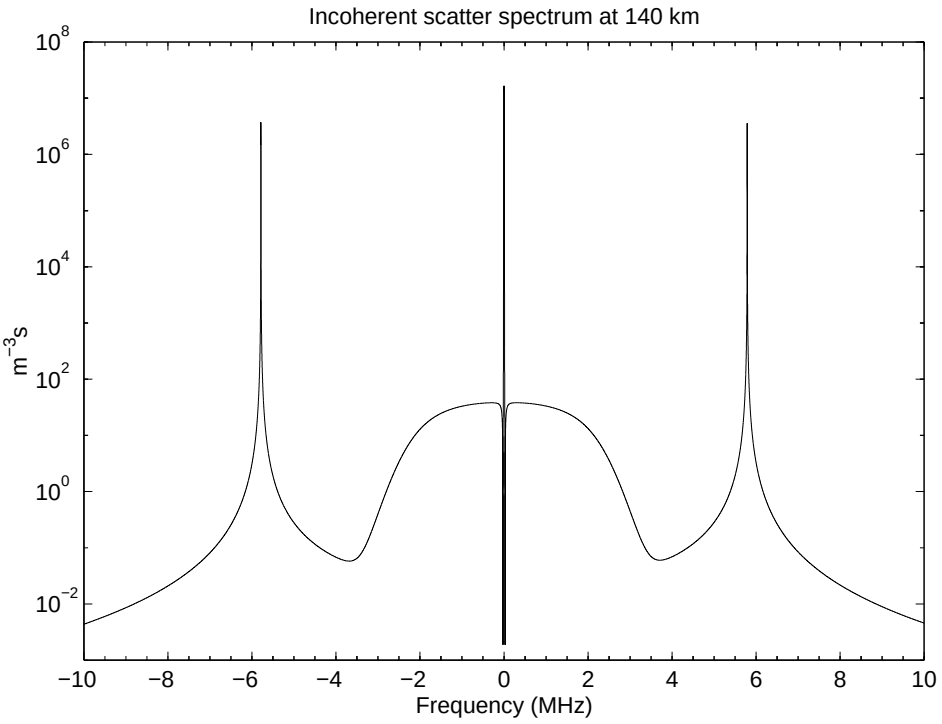

Fig. 8. The wide frequency incoherent scatter spectrum. The parameters used: $N_e = 4 \cdot 10^{11}$ m^{-3}, $T_e = 700$ K, $T_i = 600$ K, $v_i = v_e = 0$ ms^{-1} and collision frequencies ν_e and ν_i using the MSIS90e model (Hedin, 1991) for 140 km altitude. Logarithmic scale for the strength is used to be able to emphasise the different lines of the spectrum.

can nevertheless look at the different distributions in height and power for the different lines to get an idea of their nature, using the on-line integration time of 5 seconds.

The altitude distributions for the different frequencies are shown in Fig. 11. One must note that the signal levels shown are not corrected for range, as the scattering volumes are not known, so signals from a higher altitude are in fact stronger than the corresponding signal from a lower height. It is clearly seen that the strongest signal is the 5.5 MHz line, followed by 6.5, 4 and 3 MHz. The altitude distribution shows more or less the expected dependence on range, but there are some exceptions: In one point at 188 km in the 3 MHz band and for the 5.5 MHz band the strong values between 130 and 140 km seem to be stronger than the others, even taking into account the range effect. However, the number of points are too few to be used as evidence on altitude effects. Most of the echoes are coming from around 120-150 km altitude and Fig. 12 shows a simulation of the expected strength of the plasma line for given background electron density. It shows a peak at around 5.5 MHz and this is also what the experiment shows. A more realistic suprathermal distribution will decrease the returned power for a number of frequencies and one should see the figure as an upper-limit estimate. Indeed, Nilsson et al. (1996b), have made predictions of the expected strength of Langmuir waves for different heights and carefully derived distributions. These predictions are in rather good agreement with the present measurements showing a strong peak between 5 and 6.5 MHz. Although there is some uncertainty on the scattering volume, the observed strengths of the plasma lines can be used to get some estimates of the distribution of the suprathermal population. Assuming a width of 6 eV, one need, to get to the measured strengths for the 3 MHz case, a suprathermal density of about $5 \cdot 10^8$ m^{-3} which is 0.5 % of the thermal population. For the 5.5 and 6.5 MHz cases, it is enough with only

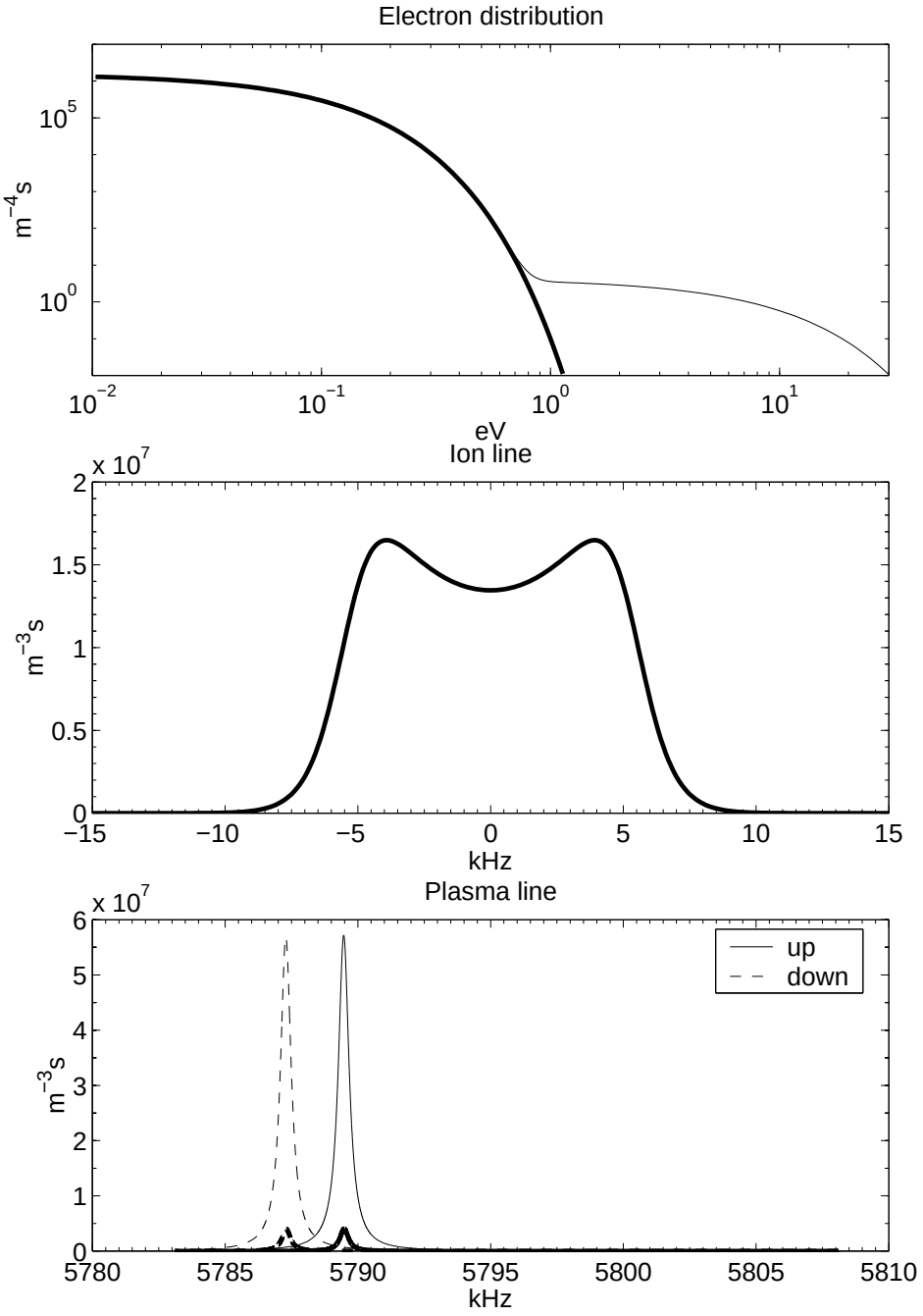

Fig. 9. Close-up of the ion and the plasma lines. Top panel shows the electron distribution, middle panel the ion line and bottom panel the plasma lines, where the frequency scale of the downshifted line have been reversed. The figure shows the lines with two different electron distributions, thick line for the normal thermal distribution and thin line for the same distribution together with an suprathermal distribution.

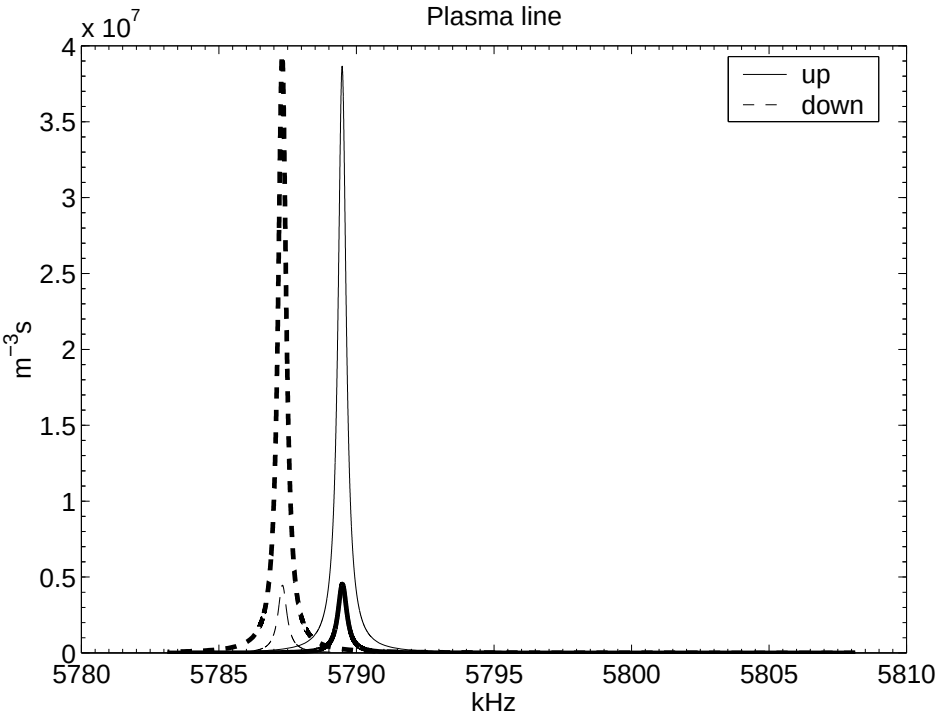

Fig. 10. The plasma lines based on an upgoing (thick line) and downgoing 10 eV beam of suprathermal electrons at a current of 1 μAm^{-2} and temperature of 5 eV. The thermal parameters are the same as in Fig. 8

$1 \cdot 10^8$ m^{-3}, but the uncertainty of volume is even larger here due to the active environment and the values should maybe be the same as for the lower frequency offsets.

The most interesting thing with incoherent plasma lines is, of course, the possibility to derive differential drifts between ions and electrons, and from these deduce ionospheric currents. For this, one needs to measure the up- and downshifted lines simultaneously. Although the time of the measurement for both lines were not exactly the same in this experiment, the time shifts between them are so small (3-6 ms) compared to the total cycle time (300 ms) of the codes, that this effect is of minor importance. In Fig. 13, the strengths and altitudes of the two concurrently recorded up- and downshifted plasma lines are shown. In general, there are stronger up- than downshifted lines for the 3 MHz case, whereas no such trend can be seen in the 6.5 MHz band. However, there are exceptions to these overall trends and on occasions there are large differences in the signal strengths between the lines. Almost all of the 3 MHz plasma lines were recorded in diffuse aurora and this evident difference in signal power needs a closer examination. When there is a drift of the thermal electrons, the plasma lines shift, and when probing at a fixed frequency, the scatter may not come from the same altitude for the up- and downshifted lines respectively. The strength of the plasma line is also rather altitude dependent due to the damping by the collisions of electrons with ions and neutrals. But Fig. 13 shows no general height difference between the up- and downshifted 3 MHz lines, so this difference in strength cannot be explained by thermal electron bulk drifts. To simulate the effect of current carried by suprathermal electrons, Fig. 14 illustrates the strength of the 3 MHz plasma lines for Maxwellian electron beams of different energies. With no net current the lines are of almost the same strength, and the difference is mainly dependent on where in the receiver band the lines are. However the experiment shows stronger upshifted lines, thus it is evident that the diffuse aurora this night contained fluxes

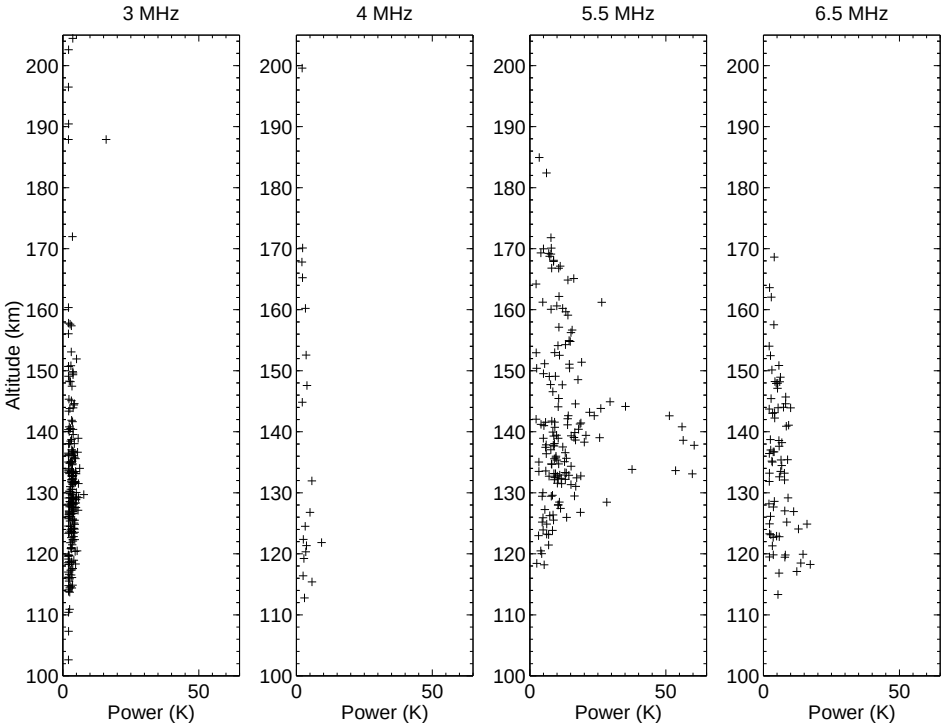

Fig. 11. Scattered plots of echo altitude and strength for the different frequency shifts. The altitudes range from 100 to 210 km, E and lower F region.

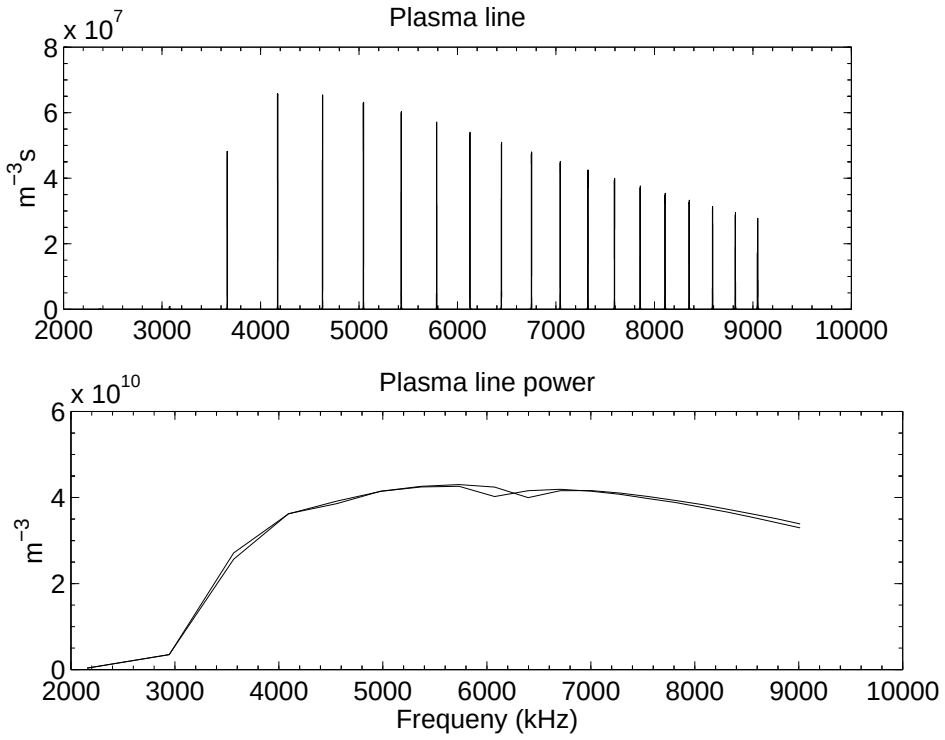

Fig. 12. Simulation of the plasma line strength at 140 km altitude with an added distribution of secondaries for different electron densities from 0.5 to $10 \cdot 10^{11}$ m^{-3}. The envelope in the lowest panel shows the total power of the plasma lines versus the Langmuir frequency.

of downgoing suprathermal electrons or, in other words, there was an upgoing current carried by suprathermal electrons. The average power ratio between up- and downshifted lines, 1.4, can be used to estimate the amount of current carried by the suprathermals. As before, using a density of $5 \cdot 10^8$ m^{-3} and temperature of 6 eV, and shifting this population to a current density of 15 μAm^{-2} brings to the observed ratios. This current seems somewhat high, but not unrealistic.

For the 6.5 MHz bands there may be a slight difference with respect to the altitude, and that is most likely due to thermal currents causing frequency shifts of the plasma lines. This effect is not very clear, but as lower heights have higher density, or Langmuir frequency, and as the downshifted line is at a slightly lower height, this is most probably an effect of a downgoing current carried by thermal electrons. The correction due to heat-flow in the plasma dispersion function, discussed by Kofman et al. (1993) and confirmed later also by Nilsson et al. (1996a) and Guio et al. (1996), but not taken into account here, would also show the same effect in altitude difference between the lines. The band widths used here, 25 kHz, are much wider than the effect of heat-flow, which is less than or around 1 kHz in the F-region and much lower in the E-region, so that cannot explain the 6.5 MHz height differences. A recent paper by Guio et al. (1998) with proper calculation of the dispersion equation investigates the heat-flow and finds that it is not necessary to invoke the effect at all, but as this paper don't go to the same extreme the heat-flow has to be considered.

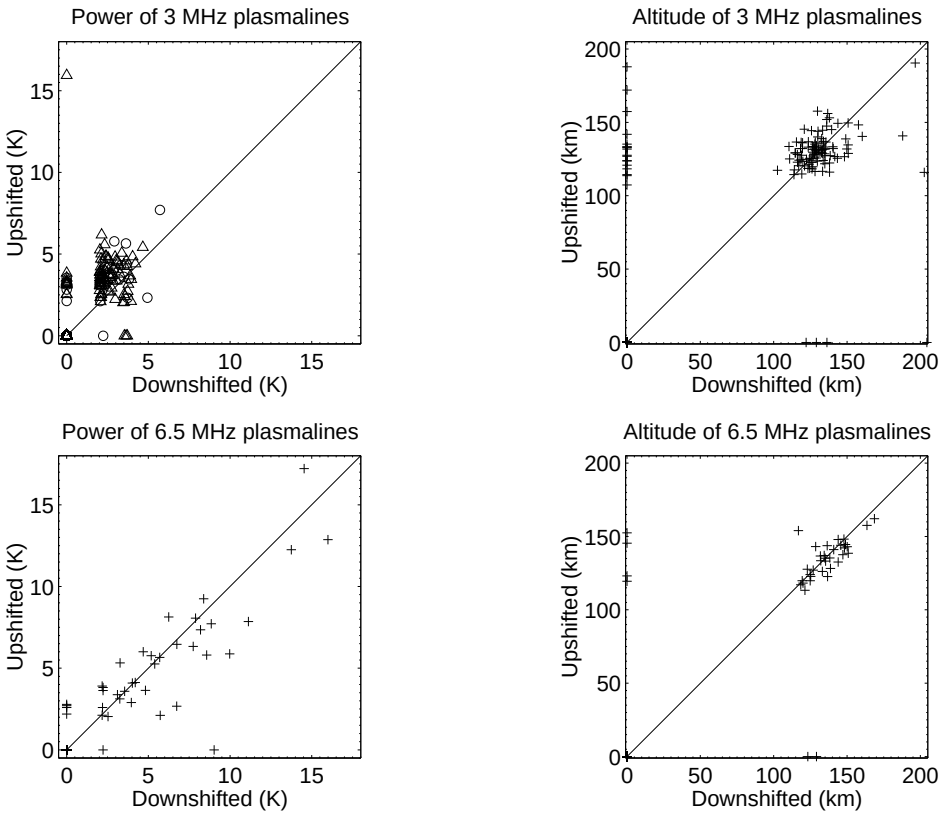

Fig. 13. Scatter plots of power and altitude for the two simultaneously measured up and downshifted lines at 3 and 6.5 MHz. The triangles and circles for the power of the 3 MHz case, in the upper left, show lines detected before and after magnetic midnight respectively — no difference can be seen.

Most of the above discussions on currents are only on directions, but to get any quantitative numbers it is necessary to look at the individual spectra. Of the 256 events of enhanced plasma lines, there is only one that is good enough

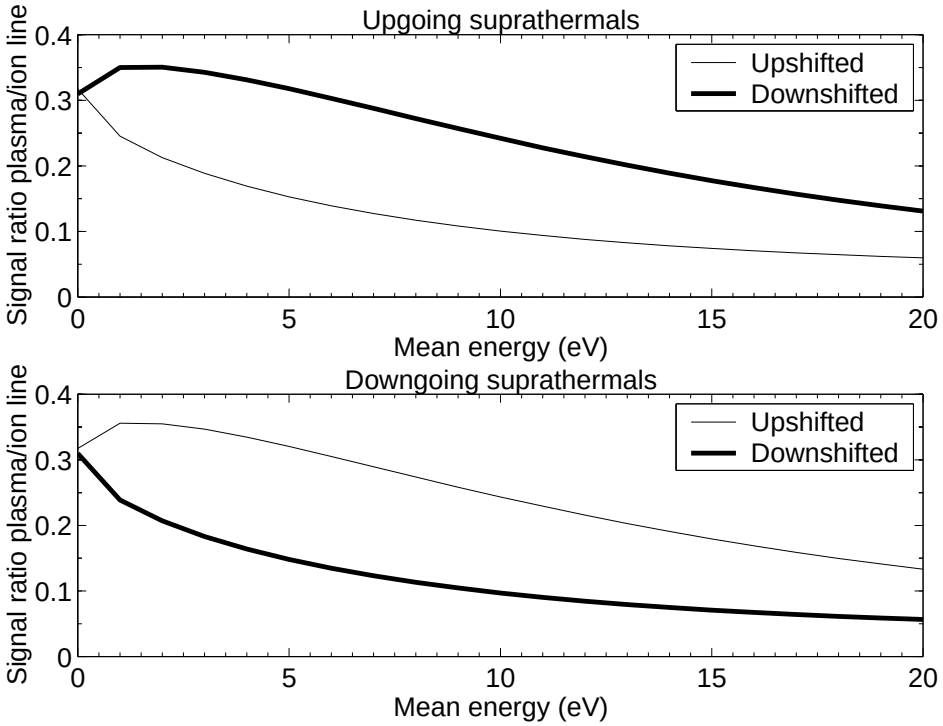

Fig. 14. Simulation of 3 MHz plasma line strength at 140 km with an electron beam with varying mean energy from 0 to 20 eV and temperature of 10 eV, corresponding to a few $\mu\mathrm{Am}^{-2}$ field-aligned currents, depending on energy. The top panel shows the ratio between plasma and ion line strengths for upgoing beams and the bottom for downgoing beams.

to investigate. All the other are too broad either due to the Langmuir frequency gradient smearing or the fact that the Langmuir frequency at the height in question is varying during the 5 second time slots. A further reason is that the stationarity condition for the alternating code technique is not fulfilled, due to changes of Langmuir frequency, and the spectra change too much within the 300 ms cycle. Anyway, there is one, and the up- and downshifted bands, together with the ion line band, are shown in Fig. 15. The shifts in this case are around 3 MHz as deduced from the ion line analysis. These spectra were then fitted to the theoretical spectrum in Eq. (7) using 7 ionospheric parameters, the thermal parameters for both ions and electrons and the parameters of a non-shifted suprathermal electron distribution. At the first glance the fit on the ion line seems rather poor, but the fit was done as usual in the time domain with proper weighting on the different lags of the ACF, and in the FFT process to produce Fig. 15 these statistical properties are lost. The fit looks actually better in the time domain, but the frequency domain was chosen in the figure to be more informative. The current density $j = N_e e(v_i - v_e)$, and with the fitted parameters, the field aligned current carried by the thermal electrons, amount to 12 $\mu\mathrm{Am}^{-2}$ downward. This is opposite the general current seen in the plasma line strength for the 3 MHz band, but the magnitudes are comparable. For this case no current could be seen on the suprathermals, and it is evident that the currents are rather structured. Of course, there are many more cases of no plasma lines than enhanced plasma lines in the diffuse aurora, and some cases of only one plasma line either up- or downshifted. It is not surprising that this single example of thermal currents do not follow the general trend. Again, heat-flow is not taken into account, but that should increase the current somewhat. The deduced suprathermal distribution is in good agreement with those Kirkwood et al. (1995) derived from the precipitating flux of primaries; of course in the present case the distribution is Maxwellian and

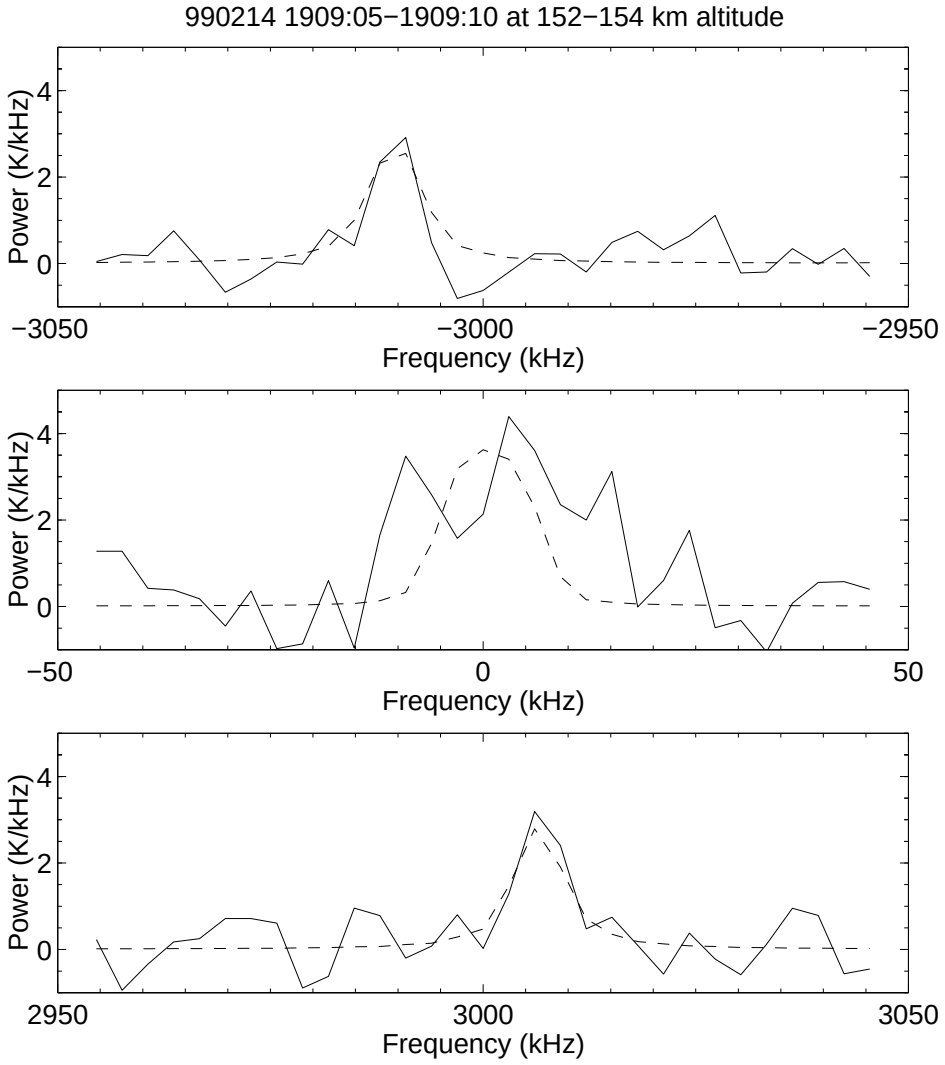

Fig. 15. Measured spectra of the both plasma lines and the ion line and the best 7-parameter fit of the theoretical spectrum. The parameters fitted were $N_e = 9.7 \cdot 10^{10}$ m^{-3}, $T_e = 631$ K, $T_i = 697$ K, $v_i = -100$ ms^{-1}, $v_e = 657$ ms^{-1} and a suprathermal distribution with $n_e = 0.8 \cdot 10^9$ m^{-3} and $T = 11$ eV.

without the fine structure due to the atmospheric constituents, but the numbers are comparable.

6 Conclusions

We have made measurements of plasma lines in the active auroral E-region. During 256 periods of 5 second integration we found a total of 468 plasma line echoes, divided into 220 on 3 MHz, 19 on 4 MHz, 157 on 5.5 MHz and 72 on 6.5 MHz. It may seem strange to try to measure plasma lines at such a low frequency as 3 MHz giving low signal levels, but in fact most of the echoes and the most interesting results came from this frequency offset.

The strongest echoes were found at the 5.5 MHz line, and somewhat weaker ones at 6.5 MHz, inside auroral arcs. One must, however, note that the strength measured inside the arcs is mostly a low-limit estimate due to the active environment. The integration period used, 5 s, is rather long in auroral arc conditions, and changes typically occur on shorter time scales. Therefore, effects of gradients in the Langmuir frequency profile, and hence scattering volumes, have not been taken into account.

The Holy Grail in incoherent scatter plasma lines is the possibility to measure currents, and in this case, the field-aligned currents in aurora. The simulations carried out here, the extended full incoherent scatter spectrum with multi-Maxwellian distributions of electrons, show that the strength of the lines is determined by the suprathermal part of the electron distribution, and the frequency mainly by the thermal part. For simultaneous up- and downshifted plasma line differences in intensity we can deduce currents carried by suprathermals, and for differences in frequency, currents carried by thermals.

The simultaneous up- and downshifted frequencies of the 3 MHz line in the diffuse aurora show, on average, an upward field-aligned suprathermal current during the two main periods when they were detected, 1940-2030 UT and 2250-2300 UT. In the arcs in general, there is an indication of downward thermal current as seen from the altitudes of the 6.5 MHz echoes. Of course, no rule is without exceptions, and there are cases where one line is much stronger than the other or the other line is not at all enhanced, indicating strong currents.

In the full 7-parameter fit of the incoherent scatter spectrum with the ion line and the both enhanced plasma lines, we obtained a thermal current with a suprathermal distribution of electrons consistent with distributions derived from precipitating fluxes.

Acknowledgements. One of the authors (I.H.) was working under a contract from NIPR and is grateful to the Director-General of NIPR for the support. We are indebted to the Director and staff of EISCAT for operating the facility and supplying the data. EISCAT is an International Association supported by Finland (SA), France (CNRS), the Federal Republic of Germany (MPG), Japan (NIPR), Norway (NFR), Sweden (NFR) and the United Kingdom (PPARC).

References

Baron, M., The EISCAT facility, *J. Atmos. Terr. Phys.*, *46*, 469–472, 1984.

Birkmayer, W. and Hagfors, T., Observational technique and parameter estimation in plasma line spectrum observations of the ionosphere by chirped incoherent scatter radar, *J. Atmos. Terr. Phys.*, *48*, 1009–1019, 1986.

Dougherty, J. P. and Farley, D. T., A theory of incoherent scattering of radio waves by a plasma, *Proc. Roy. Soc. London*, *A, 259*, 79–99, 1960.

Dougherty, J. P. and Farley, D. T., A theory of incoherent scattering of radio waves by a plasma: 3. Scattering in a partly ionized gas, *J. Geophys. Res.*, *68*, 5473–5486, 1963.

Farley, D. T., A theory of incoherent scattering of radio waves by a plasma: 4. The effect of unequal ion and electron temperatures, *J. Geophys. Res.*, *71*, 4091–4098, 1966.

Farley, D. T., Dougherty, J. P., and Barron, D. W., A theory of incoherent scattering of radio waves by a plasma: II. Scattering in a magnetic field, *Proc. Roy. Soc. London*, *A, 263*, 238–258, 1961.

Folkestad, K., Hagfors, T., and Westerlund, S., EISCAT: An updated description of technical characteristics and operational capabilities, *Radio Sci.*, *18*, 867–879, 1983.

Guio, P., Bjørnå, N., and Kofman, W., Alternating-code experiment for plasma-line studies, *Ann. Geophys.*, *14*, 1473–1479, 1996.

Guio, P., Lilensten, J., Kofman, W., and Bjørnå, N., Electron velocity distribution function in a plasma with temperature gradient and in the presence of suprathermal electrons: application to incoherent-scatter plasma lines, *Ann. Geophys.*, *16*, 1226–1240, 1998.

Hagfors, T. and Lehtinen, M., Electron temperature derived from incoherent scatter radar observations of the plasma line frequency, *J. Geophys. Res.*, *86*, 119–124, 1981.

Isham, B. and Hagfors, T., Observations of the temporal and spatial development of induced and natural plasma lines during HF modification experiments at Arecibo using chirped ISR, *J. Geophys. Res.*, *98*, 13 605–13 625, 1993.

Kirkwood, S., Nilsson, H., Lilensten, J., and Galand, M., Strongly enhanced incoherent-scatter plasma lines in aurora, *J. Geophys. Res.*, *100*, 21 343–21 355, 1995.

Kofman, W. and Wickwar, V., Plasma-line measurements at Chatanika with high-speed correlator and filter bank, *J. Geophys. Res.*, *85*, 2998–3012, 1980.

Kofman, W., St-Maurice, J.-P., and van Eyken, A. P., Heat flow effect on the plasma line frequency, *J. Geophys. Res.*, *98*, 6079–6085, 1993.

Lehtinen, M. and Häggström, I., A new modulation principle for incoherent scatter measurements, *Radio Sci.*, *22*, 625–634, 1987.

Lehtinen, M. and Huuskonen, A., General incoherent scatter analysis and GUISDAP, *J. Atmos. Terr. Phys.*, *58*, 435–452, 1996.

Mishin, E. and Schlegel, K., On incoherent-scatter plasma lines in aurora, *J. Geophys. Res.*, *99*, 11 391–11 399, 1994.

Nilsson, H., Kirkwood, S., and Bjørnå, N., Bistatic measurements of incoherent-scatter plasma lines, *J. Atmos. Terr. Phys.*, *58*, 175–187, 1996a.

Nilsson, H., Kirkwood, S., Lilensten, J., and Galand, M., Enhanced incoherent scatter plasma lines, *Ann. Geophys.*, *14*, 1462–1472, 1996b.

Oran, E., Wickwar, V., Kofman, W., and Newman, A. L., Auroral plasma lines: A first comparison of theory and experiment, *J. Geophys. Res.*, *86*, 199–205, 1981.

Perkins, F. and Salpeter, E. E., Enhancement of plasma density fluctuations by nonthermal electrons, *Phys. Rev.*, *139*, 55–62, 1965.

Rosenbluth, M. N. and Rostoker, N., Scattering of electromagnetic waves by a nonequilibrium plasma, *Phys. Fluids*, *5*, 776–788, 1962.

Showen, R. L., The spectral measurements of plasmalines, *Radio Sci.*, *14*, 503–508, 1979.

Sulzer, M. P. and Fejer, J. A., Radar spectral observations of HF-induced ionospheric Langmuir turbulence with improved range and time resolution, *J. Geophys. Res.*, *99*, 15 035–15 050, 1994.

Swartz, W. E., Analytic partial derivatives for least-squares fitting incoherent scatter data, *Radio Sci.*, *13*, 581–589, 1978.

Swartz, W. E. and Farley, D. T., A theory of incoherent scattering of radio waves by a plasma: 5. The use of the Nyquist theorem in general quasi-equilibrium situations, *J. Geophys. Res.*, *84*, 1930–1932, 1979.

Valladares, C. E., Kelley, M. C., and Vickrey, J. F., Plasma line observations in the auroral oval, *J. Geophys. Res.*, *93*, 1997–2003, 1988.

Wickwar, V. B., Plasma lines in the auroral E layer, *J. Geophys. Res.*, *83*, 5186–5190, 1978.

Paper III

Incoherent scatter spectra for non-Maxwellian plasmas

Mikael Hedin and Ingemar Häggström

Proceedings from Radiovetenskap och Kommunikation 02

Incoherent scatter spectra for non-Maxwellian plasmas

Mikael Hedin[1] and Ingemar Häggström[2]

[1]Swedish Institute of Space Physics, Box 812, 981 28 Kiruna, Sweden. E-mail: mikael.hedin@irf.se.

[2]EISCAT Scientific Association, Box 164, 981 23 Kiruna, Sweden. E-mail: ingemar@eiscat.com.

Abstract

We present an extension of the standard incoherent scatter spectral analysis. The standard assumption of the analysis is that there is only thermal electrons present in the ionosphere. This is often not the case. The major deviation from the standard spectra can bee seen in the electron line, a weak part of the spectrum between the prominent ion line and plasma lines.

This extension should be important in analysis of incoherent scatter spectra observed during conditions when there are particularly large deviations from the Maxwellian electron distribution such as during auroral precipitation, for high temperatures as obtained during ionospheric radiowave heating (HF-pumping) and at altitudes lower than 200 km all the time.

1 Introduction

The possibility to measure the scatter of radio waves from free electrons in the ionosphere using powerful transmitters and sensitive receivers was predicted in 1958[1] and the first observation was reported the same year[2]. Since then, the technique has developed into a standard instrument for space exploration, and today there are several systems around the earth in regular operation, *e.g.,* Arecibo in Puerto Rico, Millstone Hill in Massachusetts, USA and EISCAT in northern Scandinavia.

In [1] the scatter from free thermal electrons was predicted to give a weak scattered signal, Doppler broadened by the corresponding thermal motion. The first observations, however, detected a significantly stronger and more narrow signal, and it was soon realized that the full spectral shape of the return signal contained the information. In the present work we will broaden the view and again study the originally considered, wider part of the spectrum, to learn more about non-thermal conditions.

As the ionosphere is a plasma, albeit weakly ionized, the electrons do not move freely, but are coupled to the ions by the electric field. This makes the equations for the kinetic properties of electrons and ions coupled, with complex mutual dependencies. The frequency of the scattered return signal is modulated by these motions, *e.g.,* Doppler broadening and Doppler shift. Analyzing the scattered signal spectral shape it is thus possible to determine macroscopic properties of the plasma, such as electron density, ion and electron temperature and plasma drift.

2 Interpreting the incoherent scatter signal

The traditional analysis of the incoherent scatter spectra, used in routine operation of the production systems, uses the (relatively) high power part of the spectrum. The *ion line* is the central part, typically extending over several kHz around the radar transmitter frequency.[1] An example is given in figure 1.

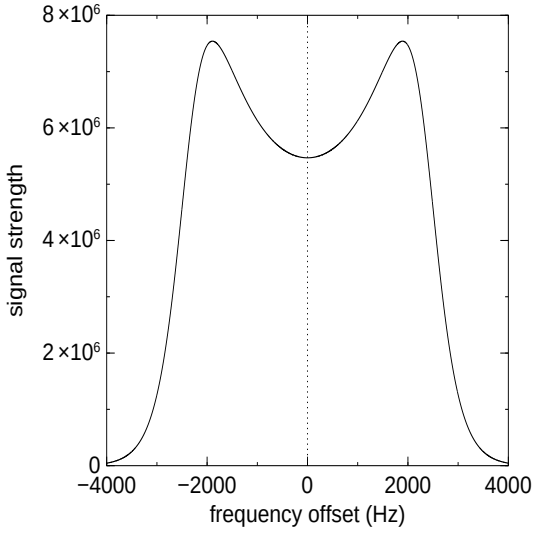

Figure 1: Signal strength for the ion line (in arbitrary units) The plasma properties are determined from the shape of the ion line, roughly as follows: the electron density is the spectral height, the first moment is the plasma drift velocity, the width depends on the ion temperature and the depression in the middle depends on electron temperature and collision frequency.

[1]The width of the scatter lines all depends on the transmitter frequency, and is given here for the EISCAT VHF system at 224 MHz

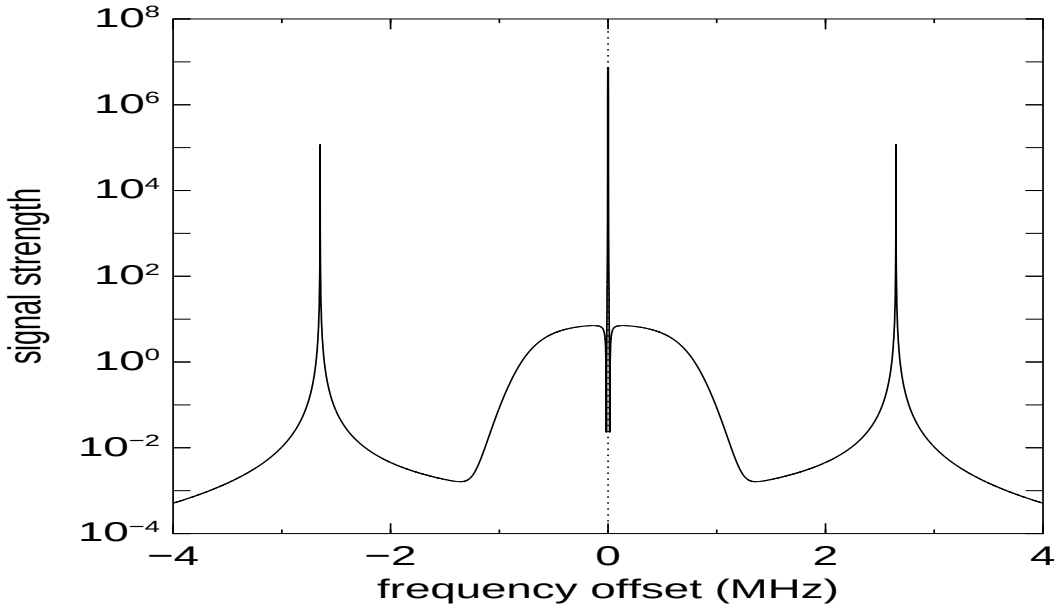

Figure 2: The incoherent scatter spectra for thermal conditions. From the center and out, we see the narrow ion line, the weak electron line and the two plasma lines.

There are also often run experiments to use the *plasma line*, under some conditions a strong signal, narrow in width and located at offsets from the transmitter frequency close to the plasma frequency. A typical offset value is $\pm 3\,\mathrm{MHz}$, as in the example in figure 2.

The Doppler broadened scatter from the free electrons at frequency offsets $\pm 1\,\mathrm{MHz}$ is called the *electron line*.[2] This part has not been used in standard operations, since the signal is difficult to detect above the measurement noise, but with recent improvements of instrument hardware, such experiments have become possible. As we will show, this part is modulated by the presence of supra-thermal electrons with energies $\approx 0.1 - 10\,\mathrm{eV}$, and strong enhancements occur for such conditions.

3 Calculating the spectra using the Nyquist theorem

Now we turn to the task of actually determining the spectra of the incoherent scatter signal. To do this, we make use of the Nyquist noise theorem. It was originated for electrical systems in [3] and generalized to arbitrary systems and dimensions in [4, 5] (not to be confused with the Nyquist theorem on frequencies).

The application of the Nyquist theorem to incoherent scatter was pioneered in a series of articles [6, 7, 8, 9, 10] for various ionospheric condition. We use these results as a basis for the current work.

[2]This value is also for the EISCAT VHF system

3.1 Summary of the theorem

The Nyquist noise theorem assumes that a generalized harmonic force F is applied to a system, and the system response is X, such that the instantaneous rate of work done by the force is $F_a X_a$ (both assumed to vary with time as $e^{-i\omega t}$ where ω is the angular frequency). If the response is linear, it can be expressed as

$$X_a = Y_{ab}(\omega) F_b, \tag{1}$$

and then, in the absence of external forces and in thermal equilibrium, there is a spontaneous response in the system, determined by the *admittance* Y of the system as

$$\langle |X_a X_b| \rangle \mathrm{d}\omega = \frac{KT}{2\pi} \mathrm{Re}[Y_{ab}(\omega) + Y_{ba}(\omega)] \mathrm{d}\omega, \tag{2}$$

where K is the Boltzmann constant and T the temperature of the system. Equivalently this can be regarded as a spontaneous action using (1). This is the thermal noise, present in all kinds of system, originating from the quantum nature of matter.

3.2 Application to the ionosphere

We regard the ionospheric plasma as a collection of separate particle populations, electrons and several species of ions, which each make up a separate system which we apply the Nyquist theorem to. Here we use vector notation, as we use three dimensions, and we are only interested of the response in the direction of the applied force so no tensor is needed[10]. We use

the definition of the admittance and the continuity equation for each population:

$$N\vec{u} = Y(\vec{F} + q\vec{E}), \tag{3a}$$

$$\Delta N = N\vec{k}\cdot\vec{u}/\omega, \tag{3b}$$

and the poison equation for the electric field

$$-i\varepsilon_0\vec{k}\cdot\vec{E} = \sum q\Delta N. \tag{4}$$

where k is the wave vector and the summation is over all species.

The incoherent scatter cross section is

$$\sigma\,\mathrm{d}\omega = r_\mathrm{e}^2\langle|\Delta N_e|^2\rangle\mathrm{d}\omega, \tag{5}$$

where r_e is the classical electron radius. Together with (3) and (4) this evaluates to

$$\sigma = \frac{N_e r_\mathrm{e}}{\pi\omega}\left\{\left|\sum_j \mu_j y_j + ik^2{\lambda_D}^2\right|^2 \mathrm{Re}\{y_e\} + |y_e|^2\sum_j \eta_j\,\mathrm{Re}\{y_i\}\right\} \cdot\left|y_e + \sum_j \mu_j y_j + ik^2{\lambda_D}^2\right|^{-2} \tag{6}$$

where

$$\eta_j = N_j {q_j}^2/N_e e^2 \tag{7}$$

and

$$\mu_j = \eta_j T_e/T_j \tag{8}$$

and the index j stand for the different ion species. Here we use the normalized admittance y, defined as

$$Y_k = \frac{N_k\omega y_k}{k^2 K T_k}. \tag{9}$$

In this form we have neglected the bulk drift of the different species, which will change ω to $\omega - \vec{k}\cdot\vec{v}$ in (3b), and hence (6) and (9) will have to be modified appropriately.

The admittances are calculated from the Boltzmann equation, and forms for different assumptions can be found in the references in section 3, *e.g.,* the appendix in [7].

3.3 Extending to multiple electron distributions

In the ionosphere, the relaxation time for the plasma is long, *i.e.,* the particles interaction in a thermal sense is very weak, and the equilibrium condition is not very strict. As the plasma is normally stationary on a time scale of seconds, a long time compared to the radar probings, we can allow the populations to have different thermal properties, *e.g.,* temperature (T) and bulk drift velocity ($\vec{v}$). As we assume thermal equilibrium for the individual populations, their particle distribution will be Maxwellian:

$$f_0 = N_0\sqrt{m/2\pi KT}\,e^{-m\vec{v}^2/2KT}. \tag{10}$$

This also applies to the electrons if we have a quasi-stable distribution which is not strictly thermal, *i.e.,* not Maxwellian. Then we can regard it as several "species" of electron, which together constitute the present distribution. We then extend (3) and (4) to also apply for the different electron populations.

The resulting cross section is then

$$\sigma = |R|^{-2}\sum_e\left\{\left|R - \frac{{q_e}^2 N_e y_e}{T_e}\right|^2\frac{N_e y_e^R}{\omega} + \left|\frac{q_e N_e y_e}{T_e}\right|^2\left(S - \frac{{q_e}^2 N_e y_e^R}{\omega}\right)\right\} \tag{11}$$

where superscripted y^R denotes the real part of y and we use the shorthands

$$R = \sum_e \frac{N_e y_e {q_e}^2}{T_e} + \sum_i \frac{N_i y_i {q_i}^2}{T_i} + i\varepsilon_0 k^2 K \tag{12}$$

and

$$S = \sum_e \frac{N_e y_e^R {q_e}^2}{\omega} + \sum_i \frac{N_i y_i^R {q_i}^2}{\omega}. \tag{13}$$

4 Comparison of the spectra

To compare these new spectra with the traditional results, we use data from Monte Carlo simulations of the electron distribution during a HF-pump situation at auroral latitudes, *e.g.,* relevant for EISCAT experiments[11]. The modification of the electron distribution is caused by inelastic collisions of electrons of energy 2–4 eV , mainly with N_2, to such high degree that the results is a significant deviation from the Maxwell distribution in the range 1.5 to 5–7 eV, as shown in figure 3.

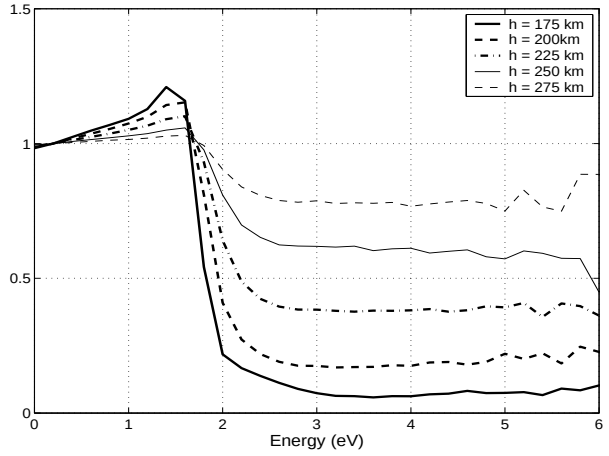

Figure 3: Quotient of the distribution of a pure Maxwellian distribution and the modeling results for several heights.

In the spectrum in figure 4 we see that the ion and plasma lines are not affected much, but the electron line is enhanced by 4 orders of magnitude at it's peak. This is such a significant difference that it should be possible to distinguish the signal from the background noise, that would hide the non-enhanced electron line.

5 Experimental evidence

To test these theoretical predictions, an special purpose program has been written for the EISCAT VHF system in Tromsø, named ELIN. This experiment was run during two periods in 2001, together with the Heater and the UHF system in a regular mode. The experiment uses a 2.5 MHz wide receiving band, with the sender frequency 0.25 MHz from the lower edge, to make sure the higher half part of the electron line falls completely in the receiving frequency band.

The data from a one minute integration in figure 5 shows that there probably is an electron line present. However, we cannot be sure that the heating really happened in the measuring range at this particular time, and if increased temperature was produced of not. To get a quantitative measurement, the temperature increase from the heater must be larger, and at the right height. It might also be possible to make a longer integration, but that requires the ionospheric conditions not to change as to destroy or alter the electron line signal.

Acknowledgement

The authors thanks Dr. Björn Gustavsson, NIPR, Japan for valuable discussions and comments on this work.

The EISCAT Scientific Association is supported by the *CNRS* of France, the *MPG* of Germany, the *PPARC* of the United Kingdom, the *NFR* of Norway, the *VR* of Sweden, the *SA* of Finland, and the *NIPR* of Japan.

References

[1] W. E. GORDON. Incoherent scattering of radio waves by free electrons with applications to space exploration by radar. *Proc. IRE*, 46:1824, 1958.

[2] K. L. Bowles. Observation of vertical-incidence scatter from the ionosphere at 41 Mc/sec. *Phys. Rev. Lett.*, 1(12):454–455, December 1958.

[3] H. Nyquist. Thermal agitation of electric charge in conductors. *Phys. Rev.*, 32:110–113, July 1928.

[4] Herbert B. Callen and Richard F. Greene. On a theoreme of irreversible thermodynamics. *Phys. Rev.*, 86(5):702–710, June 1952.

[5] Richard F. Greene and Herbert B. Callen. On a theoreme of irreversible thermodynamics. II. *Phys. Rev.*, 88(6):1387–1391, December 1952.

[6] J. P. Dougherty and D. T. Farley. A theory of incoherent scattering of radio waves by a plasma. *Proc. Roy. Soc. London*, A, 259:79–99, 1960.

[7] D. T. Farley, J. P. Dougherty, and D. W. Barron. A theory of incoherent scattering of radio waves by a plasma: II. Scattering in a magnetic field. *Proc. Roy. Soc. London*, A, 263:238–258, 1961.

[8] J. P. Dougherty and D. T. Farley. A theory of incoherent scattering of radio waves by a plasma: 3. Scattering in a partly ionized gas. *J. Geophys. Res.*, 68(19):5473–5486, 1963.

[9] D. T. Farley. A theory of incoherent scattering of radio waves by a plasma: 4. The effect of unequal ion and electron temperatures. *J. Geophys. Res.*, 71(17):4091–4098, 1966.

[10] W. E. Swartz and D. T. Farley. A theory of incoherent scattering of radio waves by a plasma: 5. The use of the Nyquist theorem in general quasi-equilibrium situations. *J. Geophys. Res.*, 84(A5):1930–1932, 1979.

[11] B. Gustavsson, T. Sergienko, I. Häggström, and F. Honary. Simulation of high energy tail of electron distribution function. Submitted to Adv. Space Res., 2001.

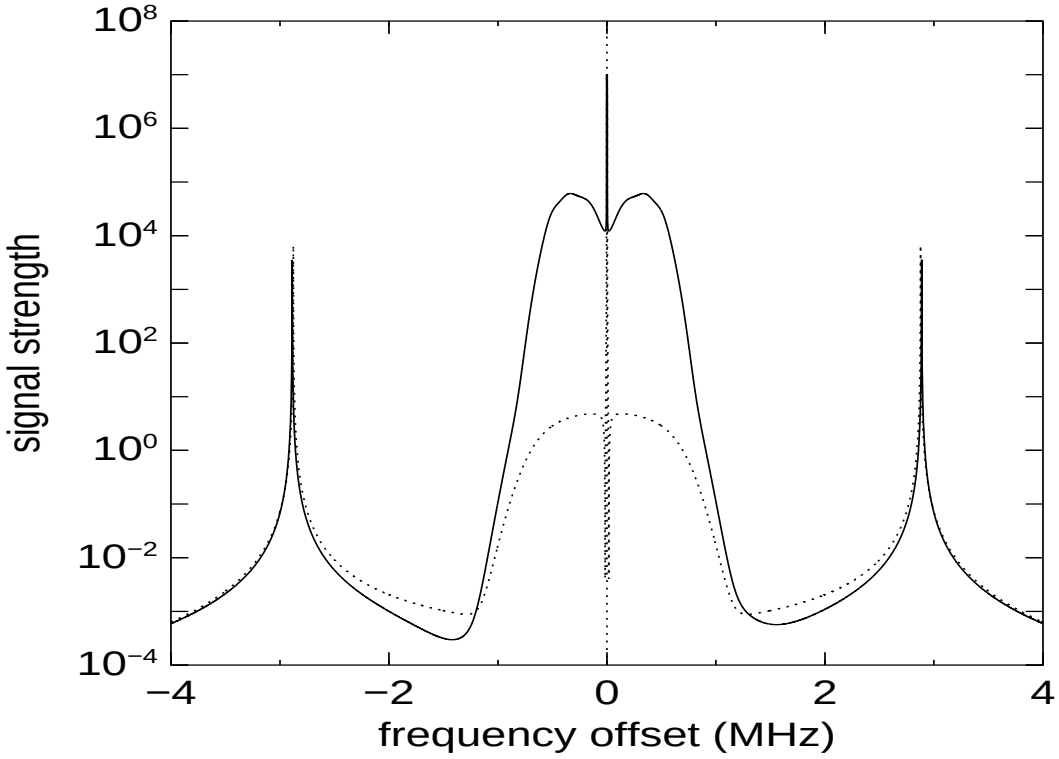

Figure 4: The incoherent scatter spectrum with enhanced electron line (full line) superimposed on an standard spectrum for the same conditions (dashed line).

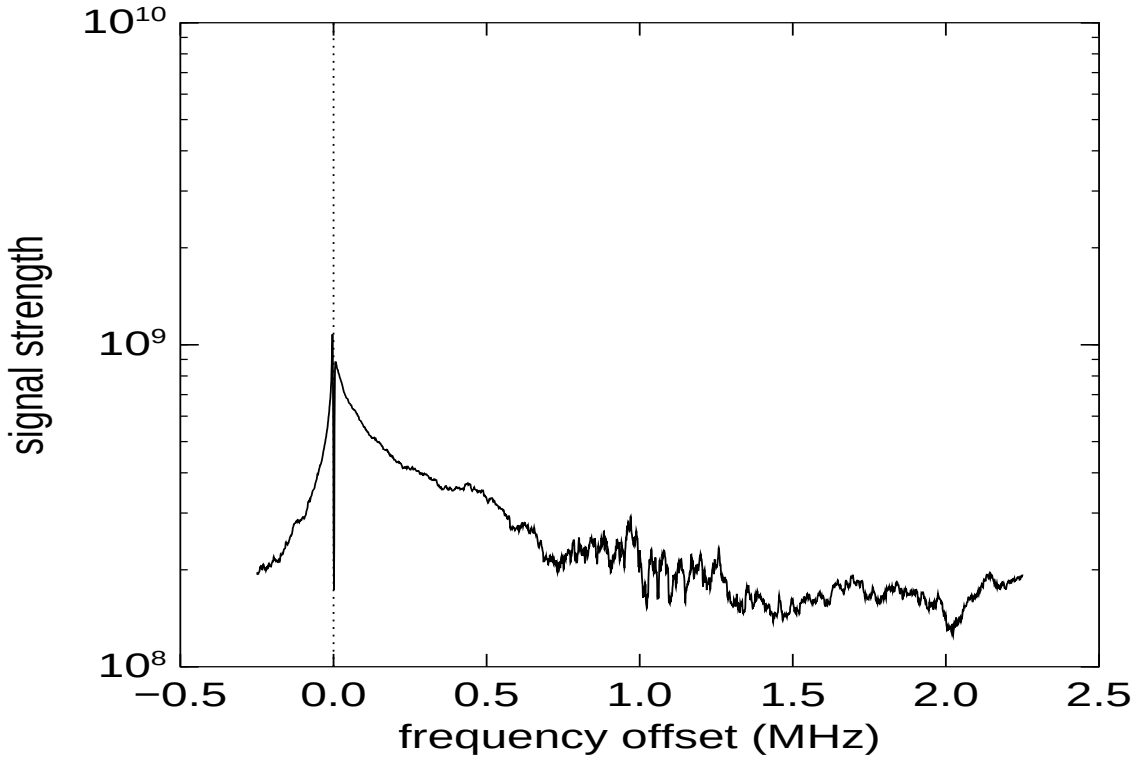

Figure 5: Data plot from the ELIN experiment ELIN@VHF 2001.10.14 18:04, integrated for 1 minute.